Mechanisms of Photoredox Catalysts: The Role of Optical Spectroscopy

Noufal Kandoth[*a], Javier Pérez Hernández[a], Emilio Palomares[a,b], Julio Lloret-Fillol[*a,b]

a. Institute of Chemical Research of Catalonia (ICIQ), The Barcelona Institute of Science and Technology, Avinguda Països Catalans 16, 43007 Tarragona, Spain.
b. Catalan Institution for Research and Advanced Studies (ICREA), Passeig Lluïs Companys, 23, 08010, Barcelona, Spain.

Abstract

The photoinduced organic transformation has stimulated the organic chemistry community to develop light-driven renewed reaction methodologies, which in many cases are complementary to standard thermal catalysis. This revitalization of photoinduced transformations is in part due to the straightforward access to powerful photosensitizers. Among those, Ru(II) and Ir(III) polypyridyl complexes have been extensively utilized as prototypical photoredox catalyst. Despite the flourish of new organic reactivity, studies of photocatalytic cycles are still scarce. The current mechanistic proposal mostly relies on luminescence quenching studies, empirical redox potentials, and bond-dissociation energy values, which provide a partial picture of the real catalytic processes occurring. Besides, quantum efficiency and overall energy efficiency of photoredox organic transformation are not usually considered merit yet. On the other hand, during the last decades, the photochemistry community has studied the energy and electron transfer mechanism of transition metal complexes from the ground and the excited-state extensively, without fully understanding the catalytic photoredox cycles probably due to its complexity. Those studies are needed to develop new photoredox organic transformations further and make them more sustainable and energy-efficient. We outline an overview of selected basic concepts of photophysics and photochemistry encountered in the photocatalytic cycles in this context. Selected examples of studies are detailed in the review to illustrate how steady-state and time-resolved optical spectroscopy can be employed to elucidate catalytic intermediates and photocatalytic mechanisms. As such, this review aims to motivate mechanistic studies on photoredox catalysis and serve as a guide to perform them to develop more sustainable and energy-efficient chemical transformations.

1. Introduction

The severe impact of fossil fuels on the planet demands urgent solutions for substituting this energy source with renewables, such as those based on solar energy. Meanwhile, photovoltaic panels directly transform solar energy into electricity, is still a subject of debate about the best energy storage solution on a large scale. In this sense, water oxidation, hydrogen evolution, and CO_2 reduction are promising approaches to convert solar energy into chemical energy, and molecular photocatalysis plays an essential role in designing and understanding these chemical transformations.[1] The photocatalytic transformation of organic molecules is also of great interest to improve our sustainability. Organic transformations also constitute a large fraction of our consumption of chemical and energy resources. Replacing thermally-driven classical large-scale organic synthesis by energy efficient photocatalytic routes could lead to a significant impact.

Harnessing photons towards useful catalytic applications has taken precedence in photochemistry research as envisaged by the Italian photochemist Giacomo Ciamician.[2] From the conversion of solar energy into added-value chemicals to greener-organic methodology, photocatalysis has attained unprecedented importance.[3,4,5] Certainly, light is the most abundant and environmentally benign energy resource, which can be used to drive endergonic reactions.[6] Using the light energy not only to activate chemical bonds but to store part of the light energy in new chemical bonds has the potential to energize chemical routes, making synthetic chemistry more energy efficient. The bioinspired blueprint for fundamental understanding and to address these aims is the natural photosynthesis, which has historically triggered research efforts on photoredox catalysis.[7,8,9,10] Organic and organometallic complexes, with appropriate electronic structure, can act as visible-light photosensitizers (PS) or photocatalysts, which harvest the visible photons and prompts electron or energy transfer to either a second catalyst or an organic substrate for further use.

Photosensitizers employed in photoredox transformations are mainly based on organic dyes,[11,12] and second, and third-row transition metal complexes with d^6 electronic configuration, such as Ru^{II}, Ir^{III}, Re^{I} and Os^{II},[7,9,13] besides copper complexes also started to appear as excellent alternative photosensitizers.[14] They exhibit tunable photoredox properties and lifetimes of electronic-excited-states long enough to engage in electron transfer (ET) or energy transfer process (EnT) via effective diffusional encounter events with other molecules. Although metal complexes derived from 3d metals are abundant and less expensive than 4d and 5d complexes, only copper(I) complexes are widely used in photoredox catalysis. Indeed, 3d

metal complexes suffer ligand lability and follow rapid excited-state deactivation pathways.[15,16,17] To solve these problems, engineering on molecular ligands by inducing, for instance, strong ligand field strength has been employed. This strategy led to discovering new metal complexes based on Cr, Mn, Fe, and Co with a similar electronic configuration like d^6 elements with relatively long lifetimes, and some of them have been successfully utilized in photocatalytic applications.[13,18,19,20]

The synthetic methodology derived from the photoredox catalysis has garnered extensive attention nowadays with an overwhelming amount of research reports on the topic.[7,8,21,22,23,24,25] Indeed, photoredox catalysis addressed to organic reactions is getting more mature, showing a plethora of new methods with a broad substrate and product scope. However, the mechanistic proposals mostly rely on fluorescence quenching studies without a backup of in-depth excited state kinetic studies or real-time elucidation of catalytic intermediates.[6,26,27,28] Therefore, a detailed understanding of the mechanisms involved is essential for further advancement in the field.[29,30,31] Further, light-driven reactions occurs through short-lived transient species, and principles of thermal reactions are not necessarily valid in photochemical reactions.[32] Hence, the conventional characterization techniques would not give the full mechanistic picture of a photocatalytic cycle.

As clean and sustainable energy became a key goal of the current century, precise information about the light absorption mechanisms, excited state decay pathways, and quantum yields are essential to design more effective photosensitizers and increase the overall energy efficiency of the reactions. Detailed understanding of the mechanisms is a tool to design strategies to improve the efficiency of the use of photons to unlock new paradigm in photoredox catalysis.[29,12] From an industrial and technological point of view, only reactions with high quantum efficiency will be likely in scaled-up applications, where the rational design of photocatalysis with a clear mechanistic understanding is the key. In this context, the present review highlights selected examples of photocatalytic systems, where the mechanism of photoinduced electron transfer processes (PET) or energy transfer process (PEnT) governing catalysis are discussed. Before this, we will briefly revisit elementary photophysical or photoredox features of inorganic complexes, especially widely utilized metal complexes. Nevertheless, detailed reviews on photophysics and photochemistry of transition metal complexes can be found elsewhere.[33,34,35,36,37]

In a simplified manner, the absorption of a UV or visible photon by a photoredox catalyst promotes a vertical electronic excitation, followed by different relaxation events. In the case of octahedral d^6 metal complexes of general photocatalysts, the essential photophysical features involved during the electron transition from a ground state to an excited energy level upon light excitation is illustrated in the molecular orbital description and Jablonsky diagram presented in Scheme 1.

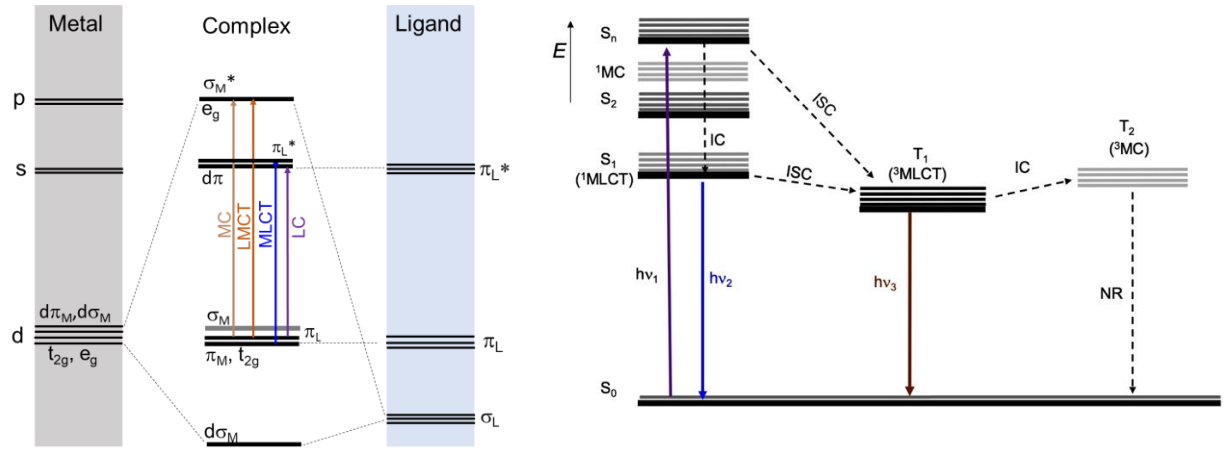

Scheme 1: (Left) Representation of molecular orbital diagram of an octahedral complex of a transition metal and its field splitting with ligands. (Right) The Jablonsky diagram of an octahedral complex showing the different transitions of energy states and relaxation processes. The arrow indicates the direction of PET into different molecular orbitals. $h\nu_1$ = photon absorption, $h\nu_2$ = fluorescence, $h\nu_3$ = phosphorescence, IC = internal conversion, ISC = intersystem crossing, MLCT, MC are metal to ligand and metal-centred ligand charge transfer, respectively, NR = non-radiative decay.

In general, molecular orbitals of metal complexes are divided into σ_L and π_L from coordinated ligands, nonbonding metal-centred π_M orbitals of t_{2g} symmetry and antibonding π_M* of e_g symmetry, respectively. Additional orbitals are the antibonding ligand-centred π_L* and metal-centred σ_M*.[32] High energy light predominantly promotes electronic ligand centred transition (^{1}LC) excitations. The LC transitions are more common in aromatic ligands with extended π-π^* orbitals, whereas MLCT is more favoured if the metal-centre can be oxidized easily and the ligand can be easily reduced. Largely employed in photoredox catalysis are the metal-to-ligand electronic transition (MLCT) and ligand to metal transition (LMCT). LMCT can be promoted when the metal is easy to reduce (or the ligand is easy to oxidize). Formally an electron from the ligand is transferred to metal centre orbitals.[32] More rarely, productive electronic transitions are the lower energy metal-centred transitions (^{1}MC), occurring from highest occupied orbital (t_{2g}) to lowest unoccupied orbital (e_g). The low energy MC transitions are frequent for first-row transition elements. Though photoexcitation process follows the above rules, the energy transitions are vastly dependent on the ligand field and molecular orbitals; therefore, they can be tuned. Further, the degenerate d orbitals of metals are destabilized and split in an octahedral ligand field termed as Δ, and this splitting depends on the ligand field strength correlated by 'spectrochemical series'.

The photophysics of transition metal complexes starts from the understanding of the electronic transitions followed by its relaxation pathways through either energy, electron transfer processes or nonradiative transitions, all-important to shed light on photocatalytic mechanisms. Additional events can

also be followed in some instances. In this direction, the review is divided into sub-sections detailing the basic photophysical processes occurring in model metal complexes (Ru and Ir complexes), and later sections will specifically address their application in photoredox catalysis with selected examples. In the final sections, we introduce briefly how these complexes' immobilization onto the heterogeneous materials governs its photochemical properties in catalytic transformations and a perspective of iron photosensitizers.

1.1 The energy transfer in photoredox catalysis

An excited-state metal complex can engage an electron transfer process (PET) or translate its excited state energy (PEnT) to a second molecule, but also unproductive deactivation pathway significantly contributes to their relaxation to the ground state via a radiative or nonradiative process. In photoredox catalysis, the main interest is to take advantage of the electron transfer process to produce chemical transformations. Nevertheless, the excited state energy transfer into an acceptor molecule results in the electronic excitation of the acceptor molecule and a concomitant decay of the metal complex to its ground state (equation 1, 2). Selected organic transformations based on PEnT are reported in Sections 2.3 and 3.1. Energy transfer could occur mainly through two different mechanisms, the so-called Förster and Dexter energy transfer mechanisms.

Förster Resonance Energy transfer (FRET, Figure 1) can be transferred between molecules at large distances (10-100 Å), providing their transition dipole moments coupled with each other. The extent of energy transfer is dependent on the distance between the donor and acceptor and spectral overlap between the emission spectra of donor and absorption spectra of the acceptor.

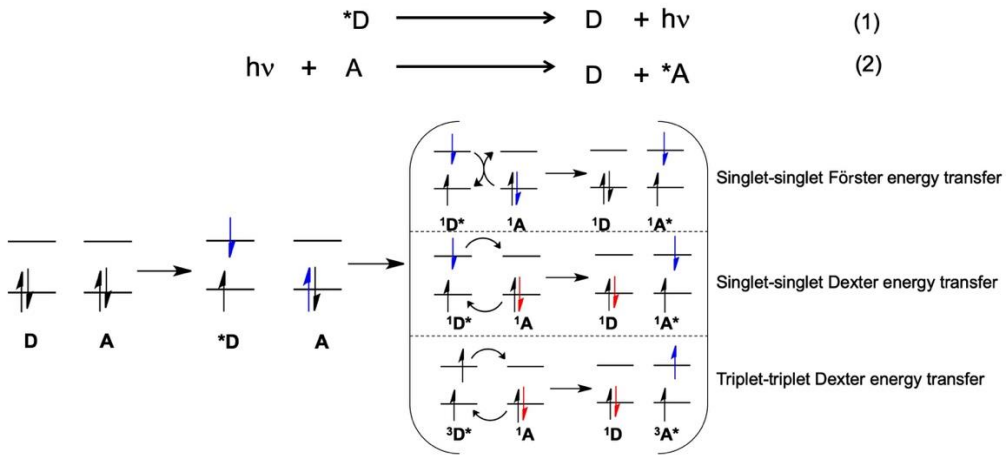

Figure 1: Förster and Dexter energy transfer mechanism operating in transition metal complexes.

When the energy transfer occurs through the electronic exchange between ground states of donor and acceptor is called Dexter energy transfer (Figure 1). To happen the electronic exchange between molecules, the overlap of the donor and acceptor orbitals must be substantial and only occurs at short distances (1-10 Å). As the hallmark of Dexter type transfer is two concomitant electron exchange with no reabsorption of emission energy by the acceptor, then the rule of spectral overlap is not required like in the case of Förster type energy transfer.[26,38] Dexter electron exchange can occur either through singlet to singlet or triplet to triplet states.

1.2 The electron transfer in photoredox catalysis

Apart from the energy transfer, photoinduced electron transfer (PET) process forms the basis of photoredox catalysis. In general, the photoexcitation of prototypical d^6-metal polypyridyl complexes promotes first the population of a singlet excited state, *i.e.* ^{1}MLCT transition. These ^{1}MLCT states then undergo deactivation via (i) nonradiative decay to the ground state or lowest ^{1}MLCT states (internal conversion, IC within the time of *ca.* 10^{-12} s), and (ii) intersystem crossing to the lowest ^{3}MLCT (ISC, in the time range of *ca.* 10^{-15} -10^{-12} s), which has an efficiency near to unity at room temperature (*eg*. Metal polypyridyl complexes like $[Ru(bpy)_3]^{2+}$ and $[Ir(ppy)_3]$). [39,40-43] The spin-orbit coupling generally causes the rapid and efficient intersystem crossing from singlet to triplet state due to the heavy-atom effect of the central metal atom.[26] Then, the radiative decay occurs from ^{3}MLCT to the ground state, called luminescence (*ca.* 10^{-9}-10^{-6} s). The ^{3}MLCT is formally a one-electron transfer from the metal (t_{2g} or π_M) to a ligand centred π^* orbital (Scheme 1, Figure 2). This gives rise to a long-lived excited state, which can undergo either an oxidation or reduction process with a second molecule of matching redox potentials.

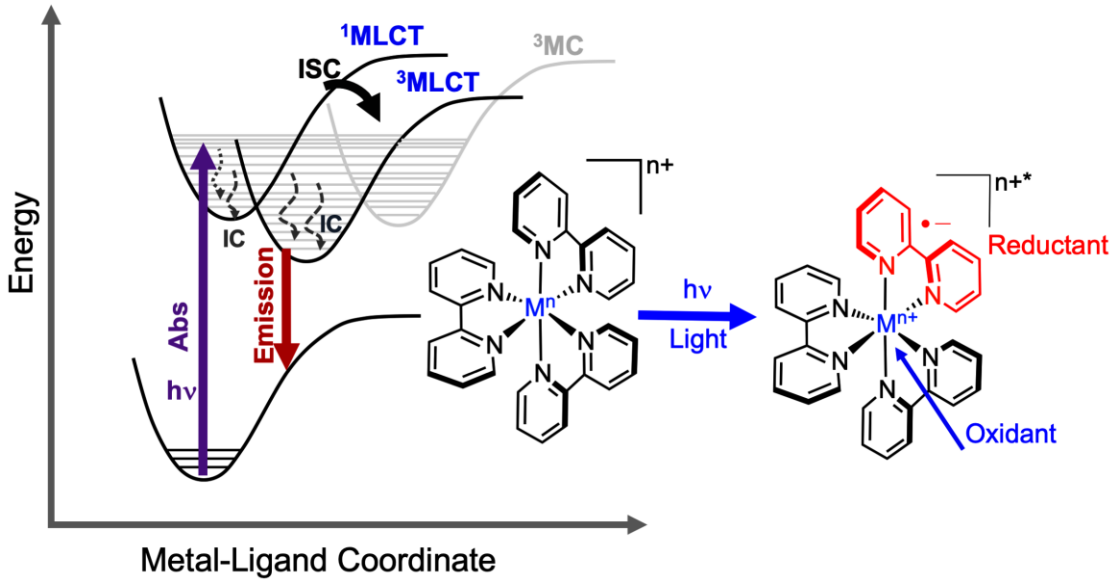

Figure 2: Simplified potential energy diagram depicting the excited-state charge transfer process occurring in metal polypyridyl complexes.

In the presence of the second molecule as an electron acceptor, the excited photosensitizer (in general $*PS^{n}$) can donate one electron to form an oxidized species (PS^{n+1}); under the oxidative electron transfer pathway (Figure 3). The oxidized photosensitizer can be reduced back to its ground state (PS) in the presence of a suitable electron-donating unit and thereby closing the catalytic cycle. Whereas in the presence of an electron-donating molecule, PS can accept one electron from the donor molecule forming reduced species (PS^{n-1}) under the reductive electron transfer pathway. This reduced species (PS^{n-1}) can oxidize back to the ground state (PS) in the presence of an electron-accepting molecule, closing the cycle. Besides, $*PS^{n}$ can also dissipate its excited state energy through an energy transfer process to a nearby molecule and go back to its ground state.

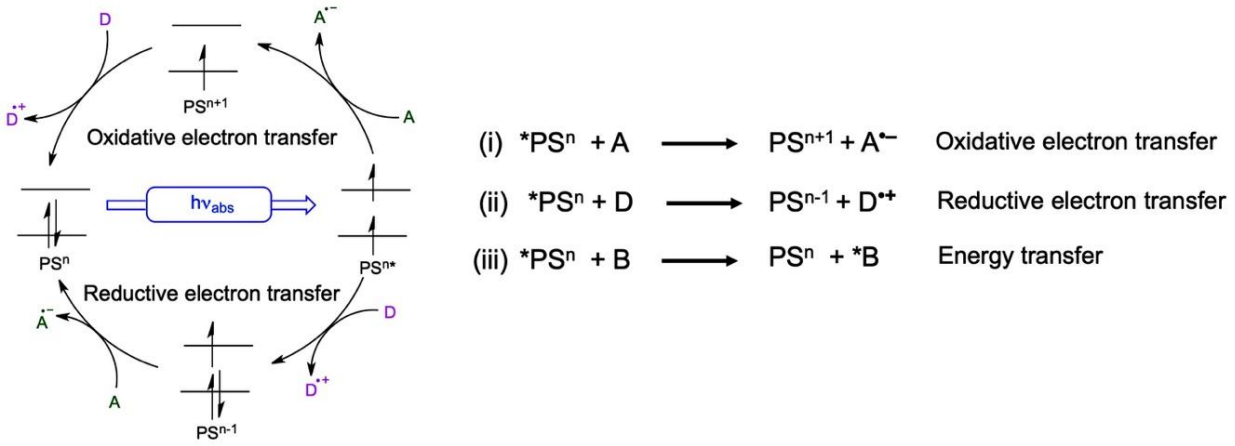

Figure 3: The oxidative and reductive electron transfer catalytic pathways for a photosensitizer in photoredox catalysis.

Although comparing the reduction potentials between PS and substrates can give an idea about the thermodynamic feasibility of an ET process, the PET kinetics between them can be more determinant. Hence, the understanding of excited-state kinetics of PS* with nearby substrates or the decay of radical intermediates is essential to optimize the photocatalysis. The lifetime of an excited state (τ), (the average time the molecule spends in the excited state prior decay back to the ground state), is another parameter that determines the excited state kinetics of the photocatalyst. Theoretically, the lifetime is represented by the reciprocal summation of all deactivation rate constants and can be measured easily by fitting exponential decay curves obtained from time-resolved emission spectroscopy. In the case of d^6-metal complexes, the lifetime decay generally occurs from ^{3}MLCT states, called phosphorescence, formed after rapid intersystem crossing from the ^{1}MLCT states.[26] The total number of emitted photons of a sample via a radiative process can be calculated from relative quantum yield, which is the ratio between absolved and emitted photons. However, the relative quantum yield can be estimated by comparing it with another emitting molecule with a known value of quantum yield under the same experimental conditions. To note, the decrease of the quantum yield of a photocatalyst, in the presence of substrates gives a first indication that catalytic reaction can occur between the excited state of catalyst and substrates.

The brief description of excited-state photophysical features described above is valid if they are present alone in a neat deoxygenated solvent (lifetime in the order of μs's). In the presence of the second molecule as electron donor/acceptor (standard case in a catalytic mixture) this excited state emission undergoes a rapid decrease in its emission quantum yield. The process at which the luminescence emission decrease is called quenching. The quenching process can occur through the so-called oxidative

or reductive quenching, depending on the oxidation state of the photosensitizer after the quenching. Alternatively, it can also occur by an energy transfer of the excited-state. There is mainly two quenching mechanism regarding the interactions between molecules involved: the so-called dynamic quenching, or collisional quenching, where the excited state collisional encounter the quencher molecule, and most relevant in photoredox catalysis. The second is the static quenching, where the luminescence emission decrease due to the formation of complexes in the ground state by the molecules (before excitation), inhibiting the formation of the excited state.[44] A typical example of collisional quenching in a catalytic mixture is the quenching of triplet excited state emission of ruthenium complexes with the molecular oxygen dissolved in the solvent. The quenching phenomena qualitatively inform on the reactivity of excited states and the quantum yield. Since it informs about the quantum efficiency of a photosensitizer, it can also be used as a benchmarking parameter to improve the energy efficiency of photocatalyzed reactions.

The Stern-Volmer quenching studies can be used to analyze the total reduction of emission quantum yield and rate of deactivation of photocatalyst with the quencher (under reductive, oxidative quenching process or during energy transfer process). For example, the total decrease in radiative quantum yield in the presence of the quencher can be calculated by Stern-Volmer equation.[38] Here, the ratio between emitter quantum yield (Φ) or lifetime (τ) in the absence or the presence of quencher correlates as follows.

$$\frac{\Phi_o}{\Phi} = 1 + K_{SV}[Q] \quad (3)$$

$$\frac{\tau_o}{\tau} = 1 + K_{SV}[Q] \quad (4)$$

Where Φ_0, Φ and τ_0, τ are the luminescence quantum yield and lifetime of the emitter in the absence or in the presence of quencher concentration [Q] and K_{SV} is the Stern-Volmer quenching constant. The K_{SV} can be calculated from the equation $K_{SV} = K_q \bullet \tau_0$, and the lifetime ($\tau_0$) is calculated from the inverse of emission decay rate constant of the emitter (K_0^{-1}), obtained by the time-resolved spectroscopy experiments. The ratio of the emission quantum yield can also be replaced with the intensity ratios at a fixed wavelength of the emission spectrum at peak intensity values if they are recorded under the same experimental settings and if the absorbance values at the excitation wavelength are the same.

In the case of a bimolecular quenching process under pseudo-first-order condition, K_{SV} is calculated from the linear plot of the ratio of quantum yield *vs.* quencher concentrations. In the case of pure of dynamic quenching, the same procedure is valid while taking the ratio of lifetime *vs.* [Q]. Further, the K_{SV} can be correlated with bimolecular quenching constant K_q by the relation $K_{SV} = K_q \tau_0$. It is important to point out

that Stern-Volmer analysis does not give any discrete analysis of the mechanism of quenching. Moreover, it gives almost indistinguishable results on electron transfer or energy transfer quenching of the excited state of the emitter. It is only the direct detection of radical intermediates by transient spectroscopic techniques that can provide a realistic picture of catalytic cycles. Nonetheless, the Stern-Volmer analysis is a valuable tool that provides a basic understanding of whether catalysis follows through oxidative or reductive quenching pathway between electron donor, photocatalyst and substrates. Apart from analyzing the quenching and getting qualitative information on the reactive excited states of photocatalyst, the quantum yield or quantum efficiency of the reaction should be high enough for an efficient photocatalytic reaction. The quantum efficiency is the ratio of the actual kinetic rate of the product formation over the amount of photon absorbed by the photocatalyst. Hence the rational design and optimization of the photocatalysis depend on extracting all kinds of kinetic rate constants pertaining to the electron transfer process (intrinsic excited state decay of PS, oxidative/reductive PET of PS and substrate, back electron transfer, slower multi-electron transfer yielding the catalysis and its turnover number) and identifying the nonproductive kinetics stopping or slowing down the catalysis.[45]

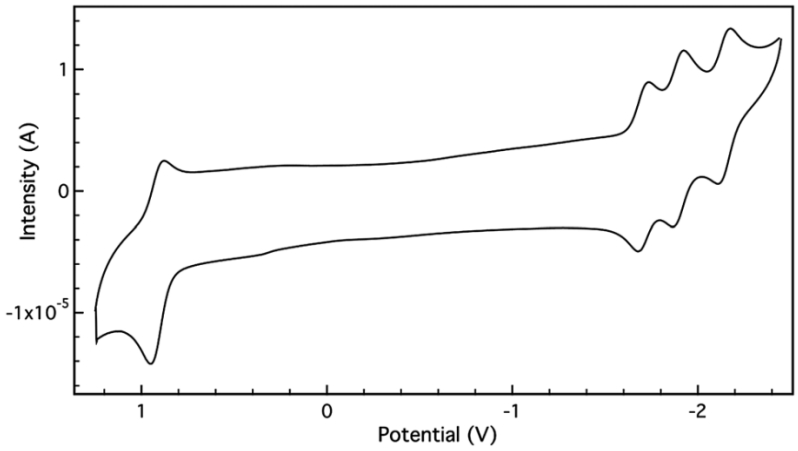

Figure 4: Cyclic Voltammogram of $[Ru(bpy)_3](PF_6)_2$ in acetonitrile using tetrabutylammonium hexafluorophosphate as supporting electrolyte. Potentials referenced to the ferrocene/ferrocenium couple (*vs.* $Fc^{+/0}$). Reproduced with permission from ref.[26].

The photocatalytic features of a photocatalyst are directly dependent on its redox potentials, and the ground state redox potential of a complex is usually determined by cyclic voltammetry. The typical cyclic voltammogram of a general Ru(II) complex that is [Ru(bpy)3](PF6)2 in acetonitrile is displayed in Figure 4. Cathodic redox events displayed in the cyclic voltammetry have been assigned to the one-electron reduction of each of the bpy ligands of $[Ru(bpy)_3]^{2+}$.[26] The oxidation potential *ca.* 0.95 V (*vs.* $Fc^{+/0}$ couple) is resulted by the oxidation of the complex to $[Ru(bpy)_3]^{3+}$. The feasibility of a photocatalytic reaction is

also dependent on the relative difference between redox potentials of donor/acceptor and excited energy of photocatalyst. For example, in order to have efficient reductive quenching of $[Ru(bpy)_3]^{2+}$ by an electron donor, the reduction potential of the donor must be lower than the $*[Ru(bpy)_3]^{2+}$ ($E^0(D^{\bullet+}/D) < E^0(*[Ru(bpy)_3]^{2+}/[Ru(bpy)_3]^{+}$). Similarly, for the oxidative quenching, the reduction potential of $*[Ru(bpy)_3]^{2+}$ should be lower than the acceptor ($E^0([Ru(bpy)_3]^{3+}/*[Ru(bpy)_3]^{2+} < E^0(D^{\bullet+}/D)$. Nonetheless, the values of the redox potentials of excited states are better determined in reaction conditions as close as the one employed during catalysis. The *in-situ* determination of the reduction potential of the excited states is somewhat complicated, but it can be estimated in two different manners. A possibility is to analyze the electron transfer rate constants of the excited state to a series of similar quenching species of known redox values.[46] The second method is empirical but practical and uses the following equations, which correlates redox potential at the excited state with the ground state reduction potentials and the excited state energy values at zero-point vibrational level ($E_{0\text{-}0}$) .[47,48]

$$E^0(PS^+/PS^*) = E^0(PS^+/PS) - E_{0\text{-}0} \quad \text{(Oxidative Quenching) (3)}$$

$$E^0(PS^*/PC^{\bullet-}) = E^0(PC/PC^{\bullet-}) + E_{0\text{-}0} \quad \text{(Reductive Quenching) (4)}$$

1.3 Energy transfer versus electron transfer

The occurrence of an energy transfer or electron transfer processes from the PS excited state to a nearby substrate or catalyst depends on the thermodynamic and kinetic feasibility of either EnT or ET in a given reaction.[26] The optical spectroscopic techniques can be employed to distinguish them in photocatalytic reactions. The most common method to interrogate the nature of quenching processes (EnT/ET) is the Stern-Volmer quenching analysis of excited emission and its lifetime decay. While the Stern-Volmer analysis distinguishes between static and dynamic quenching, as explained above, it hardly differentiates EnT versus ET.

To identify an EnT, the excited state energy ($E_{0\text{-}0}$) of a donor concerning the acceptor needs to be calculated and then determine the feasibility of the process. The $E_{0\text{-}0}$ can be assigned as the energy difference between the lowest vibrational levels of excited state and ground state (Figure 5). In a simple case, where both absorption and emission occur from the singlet state like in organic dyes, the $E_{0\text{-}0}$ can be easily obtained from the intersection point of normalized absorption and emission spectrum. To estimate the excited state triplet state energy (PEnT), this method can give unreliable results for metal complexes where the absorption and emission could arise from different excited states and often do not overlap each other. Here, PEnT is obtained by measuring T_1-S_0 energy transition *via* phosphorescence spectrum

at 77 K, where short wavelength vibrionic bands are generally assumed to represent the En_T.[49] Another practice is *via* a tangent line drawn on the high energy side of the phosphorescence spectra. As the determination of PEnT values is a challenging task, indirect methods, such as quenching experiments using a different quencher molecule with a known triplet energy levels, can also be utilized. Recently, the determination of excited state triplet energy with theoretical DFT calculation became also popular, especially with the advent of photovoltaic research.[50,51]

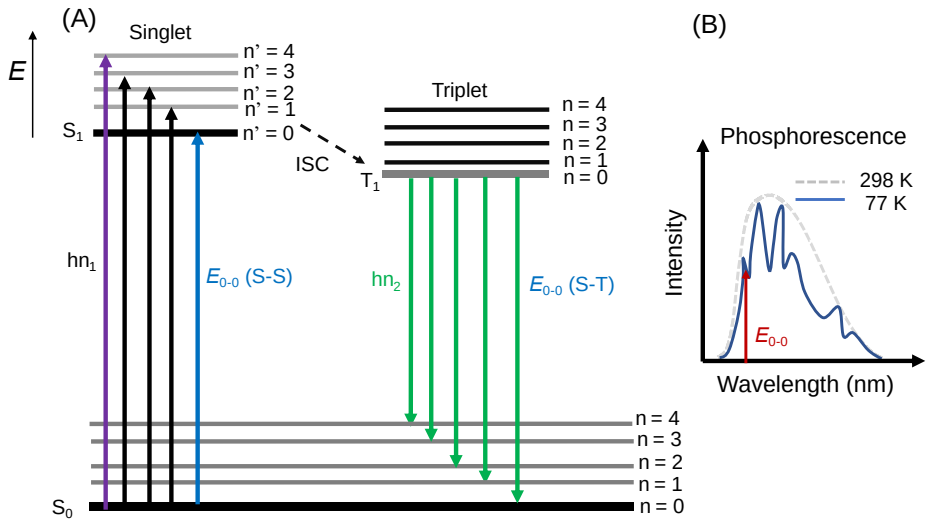

Figure 5: (A) A simplified Jablonsky diagram, showing the excited singlet state or triplet energy and including vibronic energy levels. (B) The calculation of triplet state energy from phosphorescence spectra at 77 K.

The efficiency of EnT can be correlated with the difference in their excited state energies ($\Delta E_T = E_T$ (substrate)-E_T(PS)), being the process feasible if it is exergonic ($\Delta E_T < 0$). The EnT can be further probed by transient absorption spectroscopy (see below).

1.4 Steady-state and time-resolved spectroscopy

As photocatalytic reactions involve several reaction intermediates within the catalytic cycle formed in a different time range (ps-s), they demand ultrafast absorption spectroscopy and steady-state techniques. Steady-state spectroscopic techniques such as UV/Vis absorption spectroscopy are valuable to understand photoredox catalytic cycles. For instance, UV/Vis absorption spectrum shows distinct light-absorption features and molar absorption coefficient of the photocatalyst, which in turn helps to select the appropriate wavelength irradiation sources to trigger the catalytic reactions. The absorption spectrum of a photocatalyst at the ground-state can change by the formation of adduct species with substrates, by

self-aggregation or other constituents of the catalytic medium, and then prompting the appearance of either new bands or broadening of original bands. Also, changes in photocatalyst dipole moment between the ground state and excited state can be measured in the absorption spectrum by using different polar solvents (solvatochromism). These spectral shifts are significant in transition metal complexes due to the presence of charge transfer transition between metal and coordinated ligands. The identification of reaction intermediates or products, in some cases, can be attained by monitoring the absorption spectra under steady-state irradiation conditions. However, electron transfer processes between photocatalysts and electron donor/acceptor, yielding catalytic intermediates, are in ns-μs time scale and the subsequent reactivity or recombination occurs in the μs-ms range, which is beyond the detection limit of classical UV/Vis spectrophotometer (8-10 ms time resolution). Nevertheless, the continuous accumulation of intermediates under steady-state by an external irradiation source is complementary.

Emission spectroscopy under steady-state conditions can indicate the potential reactivity of a short-living excited state with a given substrate. Luminescent quenching studies and subsequent Stern-Volmer analysis of the PS emission spectra is a simple way to start the study of the reactivity of elusive excited states. Time-resolved laser spectroscopic methods can be more informative. For instance, the time-correlated single-photon counting technique (TCSPC) can be used to measure the time-resolved emission decay of the photocatalyst in the presence or the absence of a second molecule as an electron donor or acceptor and provides an understanding of collisional quenching. In general, TCSPC measures the luminescence decay in the time domain, where the instrument registers the temporal decays of a single photon, and their time of arrival is correlated with the laser pulse used for excitation of the sample.[44] However, this technique measures only the luminescent, and the understanding of the excited state kinetics of intermediates in catalysis also requires to analyze nonemissive processes.

Transient absorption spectroscopy (TAS) is a remarkable tool to study the catalytic mechanism. An essential feature of TAS is that it has a trigger, a laser pulse. Then, the laser pulse set a temporal origin to monitor the dynamics of the absorption and emission spectra of the sample with a probe lamp and appropriate detector. In this way, the electron transfer and energy transfer kinetics of distinct transient species, generated either as initial PS excited-state or as subsequent reaction intermediates, can be monitored in a broad temporal range (ps-s timescale). The time resolution of TAS covers chemical processes of challenging access by conventional steady-state techniques or even stop-flow experiments.

The standard transient absorption spectroscopy is based on the pump-probe technique and was developed from a predecessor of flash photolysis techniques developed in 1949 by R. G. W. Norrish and G. Porter, who got the Nobel prize for this discovery in 1967.[52,53] In the pump-probe set-up, a laser

excitation source is used to excite (or pump) the sample into its excited state, and a white light source to probe the species formed after laser excitation. To analyze better signal changes associated with this technique, a differential spectrum (ΔOD) is obtained by the difference between the absorption spectrum elapsed after the laser excitation and the ground-state absorption spectrum. Therefore, the resulting signal can be positive or negative, depending on the extinction coefficient of the ground and excited states (Figure 6). The interpretation of the resulting differential spectra requires an in-depth analysis; however, few considerations can help to its interpretation.

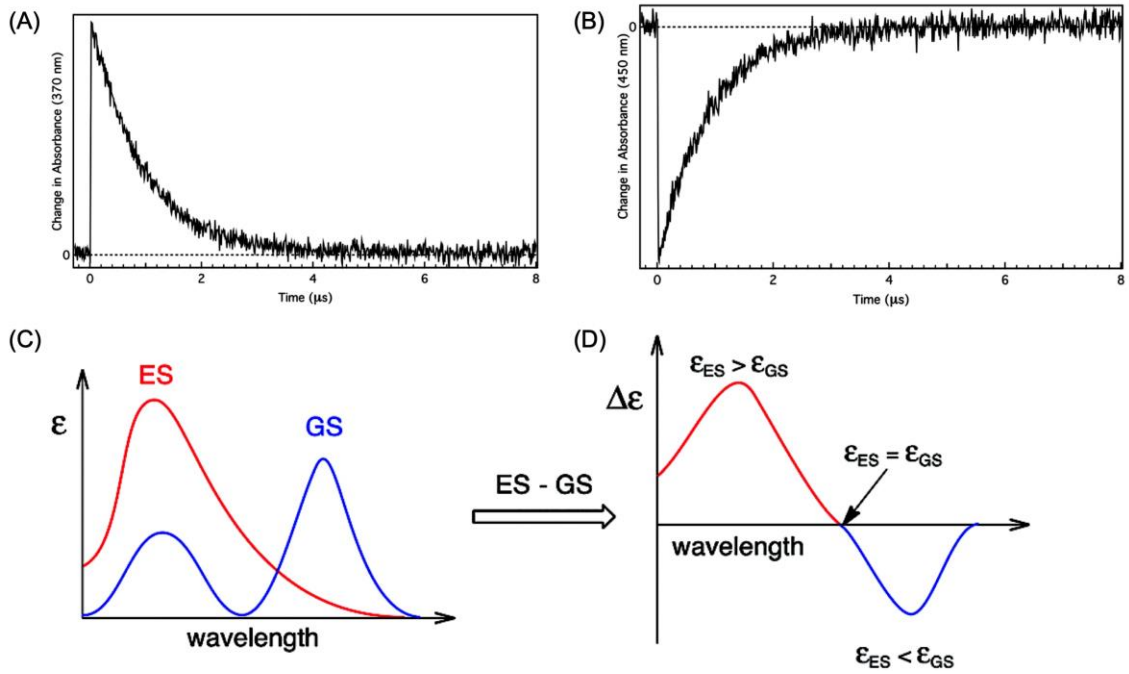

Figure 6: The transient absorption kinetics of $Ru^{II}(bpy)_3]^{2+}$ after MLCT excitation at 475 nm. (A) The positive signal refers to the reduced ligand of $Ru(bpy)_3]^{2+}$ in the MLCT excited state, and (B) The negative signal refers to the presence of Ru(III)) in the excited state (or, conversely, the loss of Ru(II) species) relative to its ground state. (C) The schematic representation of absorption spectra of the ground and excited states, and (D) the respective representation of transient absorption spectral plot. The red curve shows the positive feature and the negative feature in blue. Reproduced with permission from ref [26]

First, it should be considered that recorded TAS spectrum are not pure absorption spectrum. Besides, it is also registered the light emitted from the decay of the excited state. For untreated differential spectra, the positive absorbance values recorded are associated with the rise of new transient signals. In comparison, negative values (bleaching, ΔOD < 0) can be associated with two main reasons. The first is the consequence of the electronic excitation of the ground state to the excited state, which transforms part of the ground state into its excited state. Therefore, the absorbance value will be negative if the extinction coefficient of the generated excited-state is lower than the one of the ground-state at a given wavelength. The second possibility is a contribution of the emission spectrum from the excited state into

the absorption spectrum. Since the light is generated from the sample after laser excitation, it will appear as a negative signal. In general, for d^6 metal photoredox catalysts, the excited state decays in the ns-μs range, which is initially observed in the transient spectrum. By proper subtraction of the emission spectra obtained in TAS experiments without the probe, it can be obtained the differential absorption spectra between the excited and the ground state. If an electron transfer occurs between the excited state and a secondary molecule, the changes in the absorption spectra will be reflected in the evolution of the spectral signature from the excited state and the formed molecules. Then, the latter oxidized or reduced species could last μs-ms or longer times. Therefore, the analysis of the spectral dynamics and lifetime of the transients can help to identify processes such as vibrational relaxation, energy transfer, charge transfer, solvation, and further reactivity.

2. Ruthenium polypyridyl complex $[Ru^{II}(bpy)_3]^{2+}$ in photoredox organic transformations

$[Ru^{II}(bpy)_3]^{2+}$ (**PS_{Ru}**) is a common photosensitizer or photocatalyst employed in a multitude of transformations, including water oxidation and reduction,[41,54] CO_2 reduction,[55] and in photoredox organic transformations.[5-7] Photocatalytic **PS_{Ru}** intermediates have been extensively explored with the help of optical spectroscopic in the case of water splitting and CO_2 reductions but still did not receive the same attention as organic transformation. Nevertheless, these studies have provided complementary information about how **PS_{Ru}** can operate.

The **PS_{Ru}** absorption spectrum has a prominent LC band below 300 nm and MLCT band in between 400-500 nm (Figure 7.A).[39,56] In the presence of electron acceptors like $Na_2S_2O_8$ or other reactants, the photoexcited **PS_{Ru}** at the MLCT band undergoes oxidative electron transfer to form the one-electron oxidized $[Ru^{III}(bpy)_3]^{3+}$. The new ruthenium complex shows a characteristic absorption spectrum with a new broad band at around 650 nm (Figure 7.B). The MLCT excitation of **PS_{Ru}** in the presence of electron donors like trialkyl amines (Et_3N, triethanolamine), or reductive polyols (ascorbic acid), among other reactants, promotes the reductive electron transfer, forming the one-electron reduced $[Ru^{II}(bpy^{\bullet-})(bpy)_2]^{2+}$ complex. In this case, the absorption band presents an intense, structured MLCT band at 400 nm. The band is associated with the one-electron reduction of the bpy ligand in the $[Ru^{II}(bpy^{\bullet-})(bpy)_2]^{+}$ complex ($[Ru^{II}(bpy\text{-}CO_2Et^{\bullet-})(bpy)_2]^{+}$, Figure 7.C). Alternatively, the absorption spectrum of redox species of the photocatalyst can be generated and monitored by spectroelectrochemical methods (Figure 7.D).

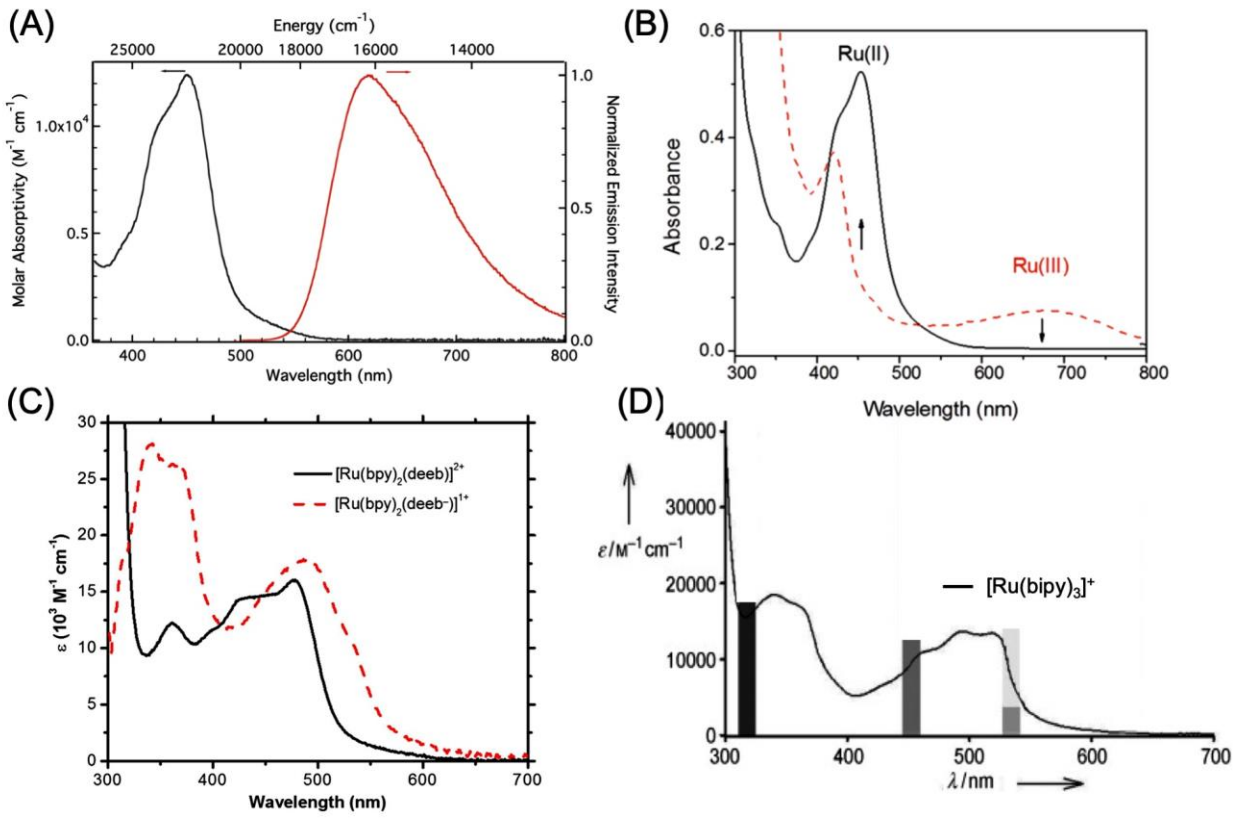

Figure 7: (A) Plot of the absorption (black) and luminescence spectrum (red) of $[Ru^{II}(bpy)_3](PF_6)_2$ in acetonitrile.[26] (B) The absorption spectrum of $[Ru^{II}(bpy)_3]^{2+}$ and $[Ru^{III}(bpy)_3]^{3+}$ formed after reaction with $Na_2S_2O_8$ under irradiation.[57] (C) Absorption spectrum of $[Ru^{II}(bpy)_2(deeb)]^{+}$, deeb= 4,4′-di-ethylester-2,2′-bipyridine (black) and its radical anion (red) formed by photoirradiation in the presence of Et_3N.[58] (D) The absorption spectra of reduced $[Ru^{II}(bpy)_3]^{2+}$ obtained by the electrochemical reduction.[59]

The electron transfer process involved in catalysis occurs in the ns-µs timescale,[60] and can be monitored by transient laser spectroscopy since the $\mathbf{PS_{Ru}}$ ground and excited state have different absorption features. Registering kinetics of the transient species at different wavelength, it has been useful to discern multiple processes, such as electron transfer, energy transfer, proton-coupled electron transfer, and hydrogen atom transfer.[39]

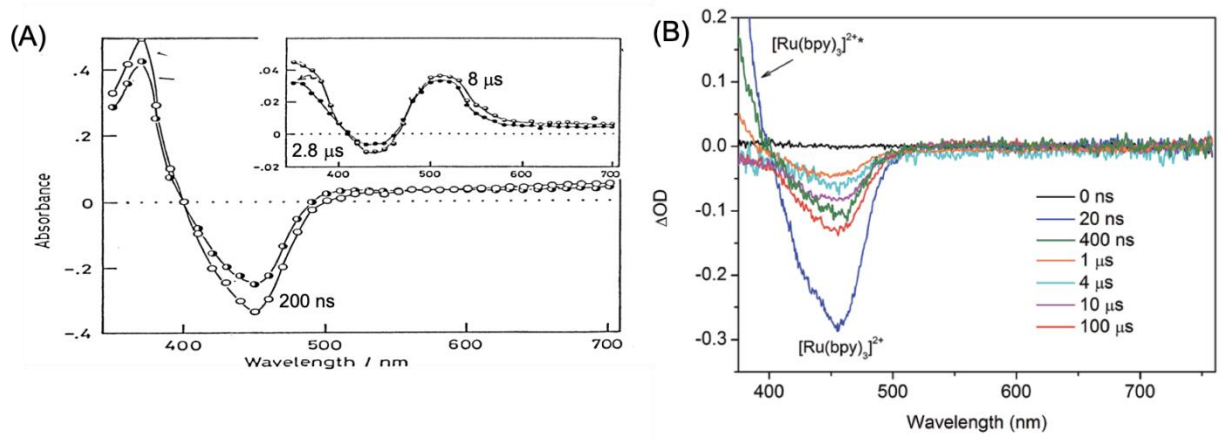

Figure 8: (A) The transient absorption spectrum (TAS) of $[Ru^{II}(bpy)_3](PF_6)_2$ in the presence of Et_3N measured at different elapsed times from laser pulse (200 ns, 2.8 µs and 8 µs) consistent with an electron transfer to the $[Ru^{II}(bpy)_3](PF_6)_2$. Reproduced with permission from ref.[61] (B) The TA spectrum of $[Ru^{II}(bpy)_3](PF_6)_2$ in the presence of $Na_2S_2O_8$ measured at different elapsed times from the laser pulse, consistent with the formation of $[Ru^{III}(bpy)_3](PF_6)_2$ *via* ET. Reproduced with permission from ref.[62]

As shown in Figure 8.A, the $\mathbf{PS_{Ru}}$ excited state absorption exhibits a feeble positive band in UV-region and a ground state bleach around 475 nm. The positive UV features are associated with the formation of the charge transfer species, the ^{3}MLCT excited state. The bleaching of the signal at 475 nm is due to the loss of ground state Ru(II) state. To note is that the ^{3}MLCT phosphorescence decay centred around 610 nm is not present in the transient absorption spectrum of Figure 8.A. The emission component of the sample can be removed by subtracting the phosphorescence spectra of the sample from the raw pump-probe spectra carefully. As in the steady-state experiments, in the presence of electron donor like Et_3N, the $[Ru^{II}(bpy^{\bullet-})(bpy)_2]^+$ ($\mathbf{PS_{Ru}}^{\bullet-}$) is formed in µs time with a transient absorption peak around 510 nm.[61] In the presence of electron acceptor like $Na_2S_2O_8$, the $\mathbf{PS_{Ru}}$ excited state is oxidized to $[Ru^{III}(bpy)_3]^{3+}$, but since its extinction coefficient is significantly smaller than the $\mathbf{PS_{Ru}}$, it is difficult to observe a positive spectral feature, except for a small shoulder in the bleaching band (Figure 8.B). The intensity of the bleaching band around 450 nm decreases following the elapsed time from the laser pulse. After 1 µs, the intensity increases as a result of the dark electron transfer between as-formed sulfate radical ($SO_4^{\bullet-}$) species and $\mathbf{PS_{Ru}}$, forming additional $\mathbf{PS_{Ru}}$ to $[Ru^{III}(bpy)_3]^{3+}$.[62] The transient catalytic intermediates obtained after oxidative/reductive electron transfer can be verified by spectroelectrochemistry experiments, where the oxidized or reduced form of $\mathbf{PS_{Ru}}$ is generated electrochemically and its UV/Vis absorption spectrum measured.[63,64]

2.1 Oxidative photoredox catalytic transformations mediated by $[Ru^{II}(bpy)_3]^{2+}$

The mechanistic elucidation of photoredox organic transformations mediated by **PS_{Ru}** using transient absorption spectroscopy is still limited. Nevertheless, some selected examples are noteworthy to be detailed. First, we introduce an example that illustrates how a PS can be studied in the context of oxidative quenching for the oxidation of an organic substrate mediated by a metal complex in a high oxidation state (Figure 9).

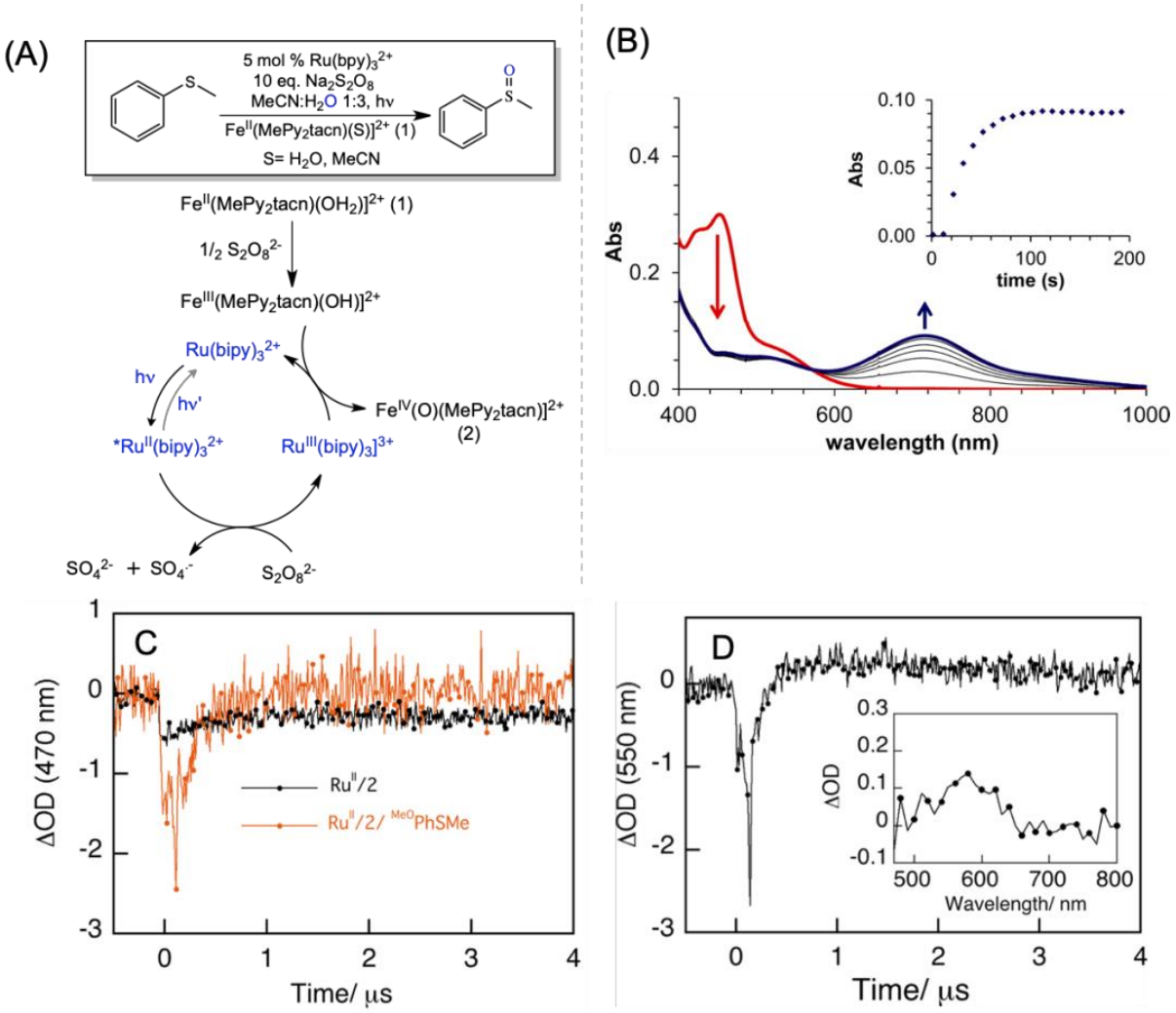

Figure 9: (A) Photocatalytic cycle generating the Fe(IV)-oxo intermediate mediated by **PS_{Ru}** and the oxidation reaction of thioanisole into sulfoxides. (B) Steady-state absorption spectra showing the oxidation of **PS_{Ru}** and concomitant formation of Fe(IV)-oxo intermediate by light irradiation (λex = 447 nm) in the presence of $Na_2S_2O_8$. Inset: kinetic trace at 715 nm. (C) Transient absorption kinetics of $[Ru^{II}(bpy)_3](PF_6)_2$ at λex = 470 nm in the presence of chemically formed Fe(IV)-oxo catalyst intermediate (2, black) and also in the presence of substrate thioanisole (orange). (D) Transient absorption kinetics at λex = 550 nm showing the formation of substrate radical cation in the catalytic mixture and its spectrum with the peak position at 580 nm. Reproduced with permission from ref.[65]

The authors showed how the **PS_{Ru}** catalytically oxidized an aminopyridine Fe(II) complex to its high oxidation state Fe(IV)-oxo species *via* an oxidative quenching mechanism using $Na_2S_2O_8$ as a sacrificial electron acceptor. Then, the generated Fe(IV)-oxo catalytic intermediate was used to oxidize thioethers to sulfoxides. Interestingly, the ^{MeO}PhSMe oxidation rate by the Fe(IV)-oxo coordination complex increases 150-fold under photoirradiation versus the reaction under dark. Kinetics experiments, monitored by UV/Vis spectroscopy under light irradiation and at steady-state conditions, were quite revealing. A mixture of $Na_2S_2O_8$, Fe(II) complex and a catalytic amount of **PS_{Ru}**, evolved to an Fe(IV)-oxo species followed by the disappearance of the characteristic MLCT absorption spectrum of **PS_{Ru}** upon irradiation. These changes suggested an electron transfer between ***PS_{Ru}** and $Na_2S_2O_8$ formed the $[Ru^{III}(bpy)_3]^{3+}$. Then, the catalytically generated $[Ru^{III}(bpy)_3]^{3+}$ oxidizes Fe(II) to Fe(III) and then to Fe(IV) as judged by the new appearance of a broad band at 715 nm (Figure 9.B). The characteristic Fe(IV)-oxo UV/Vis band quickly disappeared when introducing the substrate (*i.e.* ^{MeO}PhSMe) in the reaction mixture.

Transient absorption spectroscopy studies were illustrative to unravel the mechanism of the observed increment of reaction rate upon irradiation as described above. The transient absorption kinetics of PS_{Ru} gives a ground-state bleaching band at 470 nm, which fully recovers within 3 μs. In the presence of the Fe(IV)-oxo intermediate, the bleaching band tails up to 150 μs, assigned to the formation of $[Ru^{III}(bpy)_3]^{3+}$ since their extinction coefficient is negligible in comparison with the starting PS_{Ru}. However, in the presence of Fe(IV)-oxo and ^{MeO}PhSMe, the bleaching band at 470 nm is fully recovered in < 3 μs, but with a concomitant formation of a new long-lived positive band at around 580 nm. This new feature at 580 nm is attributed to the radical cation $^{MeO}PhSMe^{\bullet+}$ (Figure 9.B) formed by the oxidation of ^{MeO}PhSMe by the *in-situ* generated $[Ru^{III}(bpy)_3]^{3+}$. The same mechanism is also operative when $[Ru^{III}(bpy)_3]^{3+}$ is generated with $Na_2S_2O_8$.

Therefore, this study reveals a new oxidation channel for the thioether, which is different from the classical oxygen transfer mechanism from the Fe(IV)-oxo (or in general a reactive metal-oxo) to thioethers to form the respective sulfoxide and Fe(II). The new channel should imply the light promoted oxidation of the thioether to $^{MeO}PhSMe^{\bullet+}$. Then, the $^{MeO}PhSMe^{\bullet+}$ species react with the Fe(IV)-oxo intermediate to form respective sulfoxide and Fe(III). Under light-driven catalytic conditions, the latter channel was determined to be the responsible path accounting for the high rate acceleration.

The catalytic oxygenation of substrates with high valent metal-oxo species formed under photocatalytic conditions has been an active area of research before the surge of photocatalytic redox

transformations. The groups of Fukuzumi and Nam were pioneers in the photocatalytic oxygenation of inert substrates with water as an oxygen source.[66] They introduced photocatalytic olefin epoxidation, alkane hydroxylations and sulfoxidation reaction by using catalytic mixture having manganese porphyrins as catalyst ((por)Mn), **PS_{Ru}** as a PS and $[Co^{III}(NH_3)_5Cl]_2$ as weak one-electron oxidant (Figure 10).[67] The catalytic reaction mechanism was investigated with the help of transient absorption spectroscopy.

The photocatalytic oxygenation of substrates with water as oxygen donor starts with oxidative electron transfer from $[Ru^{II}(bpy)_3]^{2+*}$ to the sacrificial electron acceptor ($[Co^{III}(NH_3)_5Cl]_2$) to form the $[Ru^{III}(bpy)_3]^{3+}$. Then the $[Ru^{III}(bpy)_3]^{3+}$ oxidizes the [(por)Mn^{III}(OH)] species to the high-valent [(por)Mn^{IV}(O)] (Figure 10). A second-order kinetics for the reaction of [(por)Mn^{IV}(O)] with sodium p-styrene sulfonate (NaSS) suggested that two [(por)Mn^{IV}(O)] intermediates undergoes first a disproportionation reaction to yield $[(por)Mn^{V}(O)]^{+}$ and [(por)Mn^{III}(OH)]. The MnV-O intermediate formed via de disproportionation was proposed to oxidize the substrate (S) to yield oxygenated products (SO), together with the formation of [(por)Mn^{III}(OH)] with water (Figure 10.A).

The transient absorption spectra measured of the catalytic mixture in the μs-ms time range shows the formation of differential spectra matching with the one obtained by the chemical oxidation of [(por)Mn^{III}(OH)] with m-chloroperoxybenzoic acid to form [(por)Mn^{IV}(O)] (m-CPBA, Figure 10.B-C). In the transient absorption experiment, the laser repetition rate was remarkable slow (60-90 s) to ensure that the photochemically generated [(por)Mn^{IV}(O)] can undergo the disproportionation reaction to [(por)Mn^{V}(O)] and [(por)Mn^{III}(OH)], followed by the oxidation of NaSS with [(por)Mn^{V}(O)], regenerating all the [(por)Mn^{III}(OH)] before the new laser pulse. Later, the same group has extended this strategyto other catalyst-substrate combinations mediated by the photoredox activity of the **PS_{Ru}** for selective photocatalytic oxidations.[66,68,69,70]

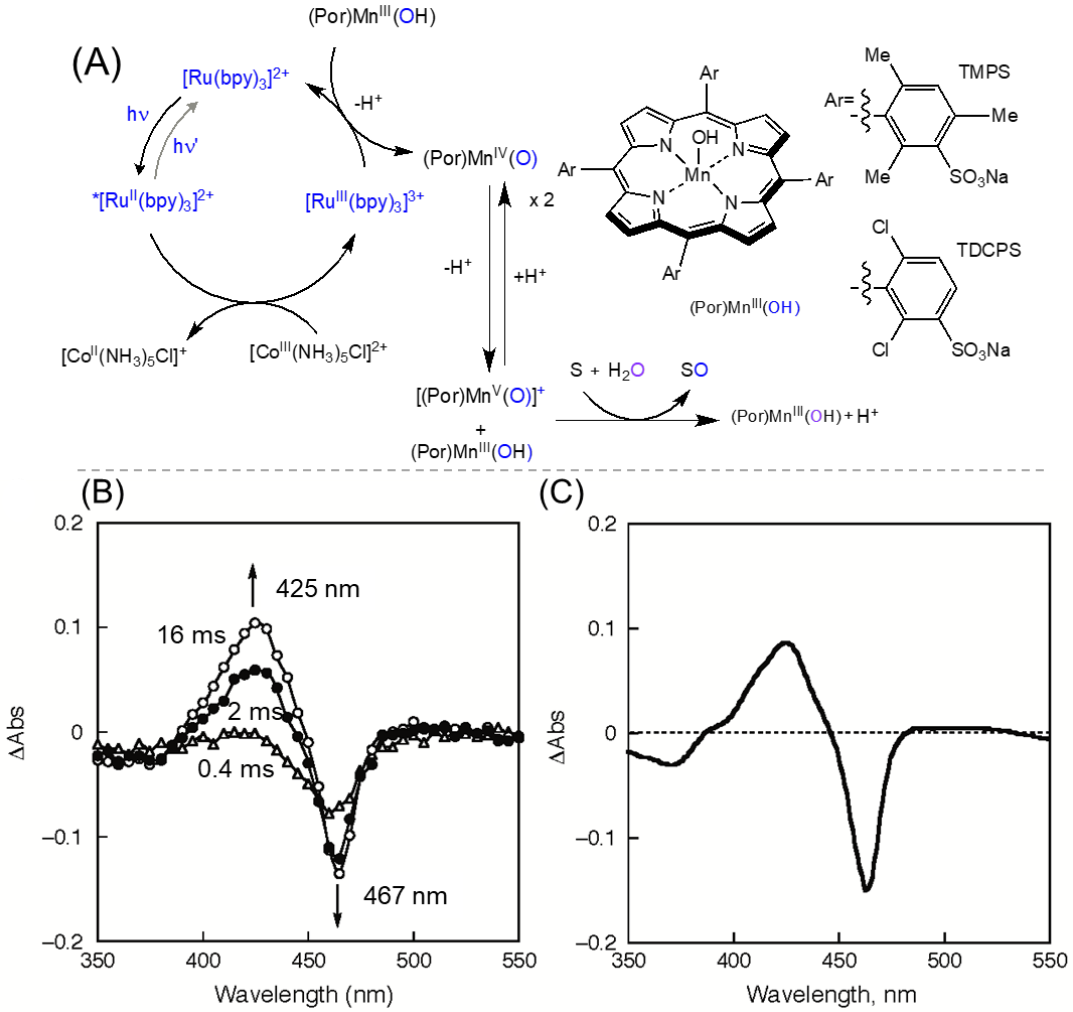

Figure 10: (A) Proposed photocatalytic cycle of oxygenation reaction where **PS_{Ru}** used as PS, [(por)Mn^{III}(OH)] as an oxygenation catalyst, $[Co^{III}(NH_3)_5Cl]^{2+}$ as a weak one-electron oxidant and water as the oxygen source, (B) The transient absorption spectra shows the formation of [(por)Mn^{IV}(O)] intermediate in a mixture of $[Ru^{II}(bpy)_3]^{2+}$, $[Co^{III}(NH_3)_5Cl]^{2+}$, [(por)$Mn^{III}$(OH)] and sodium p-styrene sulfonate (NaSS) as substrate at different delayed times from the laser pulse. (C) Differential spectrum of [(por)Mn^{IV}(O)] and [(por)Mn^{III}(OH)]. [(por)Mn^{IV}(O)] was generated by chemical oxidation of [(por)Mn^{III}(OH)] with *m*-chloroperoxybenzoic acid. [67]

Oxidation of organic substrates using directly O_2 as an oxidant is challenging; this is more challenging if the light is used as an energy source. One of the limitations is the need for a suitable sacrificial electron donor to activate the O_2 by reductive quenching of the PS. In this regard, the groups of Leibl and Aukauloo have developed a catalytic system that used methyl viologen dication (MV^{2+}) as a redox relay in combination with **PS_{Ru}** and the semi-hemic Fe^{III} catalyst to achieve the aerobic oxidation of alkenes to two oxygenated compounds (a diol and aldehyde) in an aqueous medium without the need of an additional

sacrificial electron donor (Figure 11, 12).[71, 72] The mechanism comprising three catalytic cycles (**PS_{Ru}**, MV^{2+}, Fe) was studied by transient absorption spectroscopy.

Photoexcitation with a laser pulse (λ_{ex} = 460 nm) of an oxygen-free solution containing **PS_{Ru}** and MV^{2+} showed the characteristic transient absorption spectral feature (peak c.a. 605 nm) of $MV^{+\cdot}$, and the $[Ru^{III}(bpy)_3]^{3+}$ was also detected by the bleaching kinetic at 450 nm corresponding to the disappearance of **PS_{Ru}** since the extinction coefficient of $[Ru^{III}(bpy)_3]^{3+}$ is much lower than **PS_{Ru}** (Figure 11 and step 1, Figure 12). In the presence of O_2, $MV^{\bullet+}$ decays faster than $[Ru^{III}(bpy)_3]^{3+}$, supporting the rapid electron transfer from $MV^{\bullet+}$ to O_2 forming O_2^- (step 2). Finally, the $[Ru^{III}(bpy)_3]^{3+}$ oxidant regenerate back to its ground state and close the catalytic cycle while oxidizing the substrate alkene into its radical cation. These are further demonstrated by the fast decay of $[Ru^{III}(bpy)_3]^{3+}$ in the presence of alkene and electron paramagnetic spectroscopy detection of alkene radical cation (step 4).

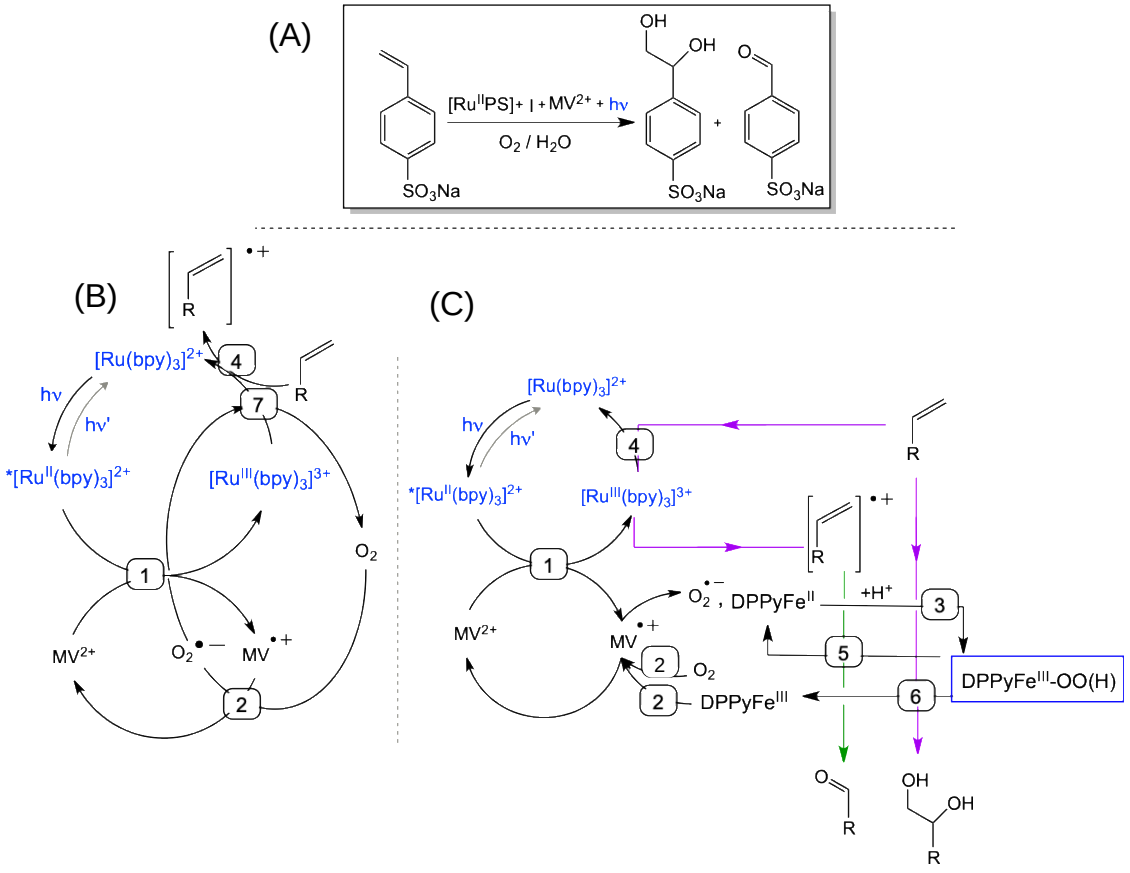

Figure 11: Photocatalytic cycle showing the oxygen atom transfer reaction of styrene sulfonate with O_2 in the absence of a sacrificial electron donor. Reproduced with permission from the ref.[71, 72]

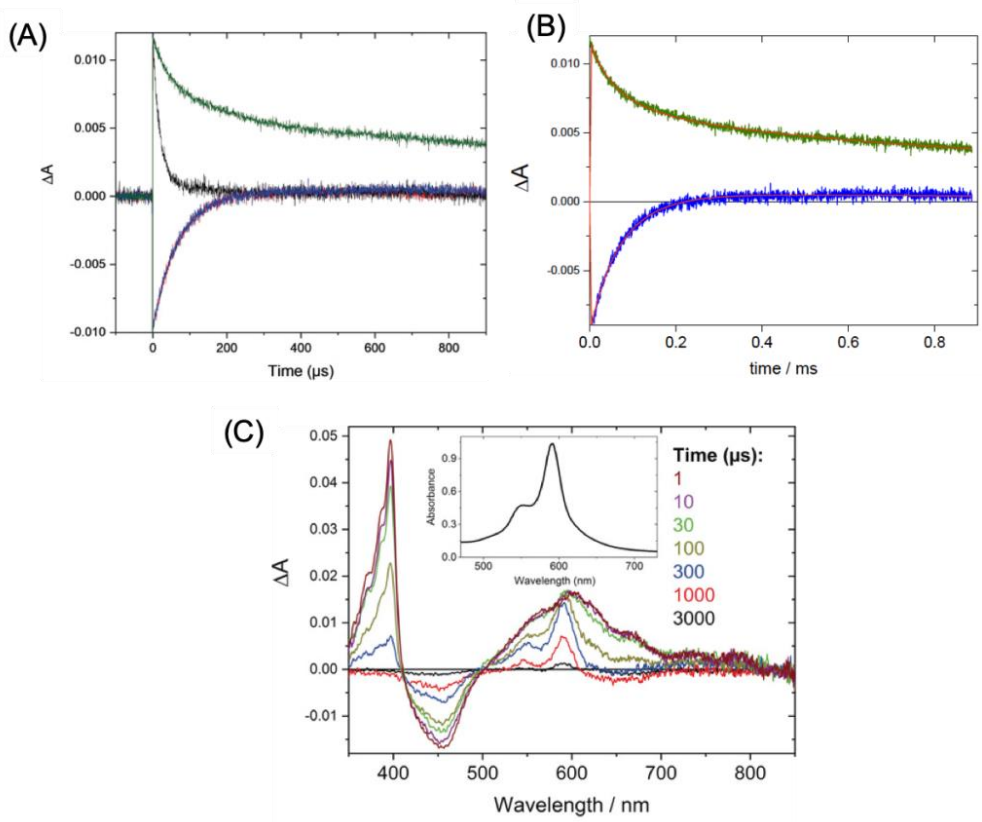

Figure 12: (A) Transient absorption kinetics of the catalytic mixture containing $[Ru^{II}(bpy)_3]^{2+}$, MV^{2+} with sodium 4-styrenesulfonate substrate at 605 (green) and 450 nm (blue) under argon; 605 nm (black) and 450 nm (red) under aerobic conditions. (B) Transient absorption kinetics of the solution containing $[Ru^{II}(bpy)_3]^{2+}$ and MV^{2+} at 605 nm (green) and 450 nm (blue) in Ar-saturated solution in the presence of sodium 4-styrenesulfonate. (C) Transient absorption spectrum from an Ar-saturated solution of $[Ru^{II}(bpy)_3]^{2+}$, MV^{2+} and the catalyst dimer[71] at the indicated delay times after laser pulse (inset) UV/Vis spectrum of $(DPPy)Fe^{II}$ in water under argon. Reproduced with permission from ref. [72]

The recovery of $\mathbf{PS_{Ru}}$ after the recombination between Ru(III)PS and $MV^{\bullet+}$ was observed to follow the same kinetics both at 450 nm ($[Ru^{III}(bpy)_3]^{3+}$) and 605 nm ($MV^{\bullet+}$) under argon. Whereas in the presence of substrate alkene, the recovery of $\mathbf{PS_{Ru}}$ was much faster than $MV^{\bullet+}$, resulting in the formation of the alkene radical cation (Figure 12.A-B). Finally, the introduction of Fe(III) catalyst, i.e. $\{[(DPPy)(EtOH)Fe^{III}]_2O\}^{2+}$,[71] under argon results in rapid consumption of the decay of $MV^{\bullet+}$ concomitant with the formation of new transient absorption band around 550 and 590 nm, corresponding to reduced $(DPPy)Fe^{II}$ (Figure 12.C). The same absorption features were also observable under air and indicated the competitive reduction of Fe^{III} catalyst *vs.* O_2 by $MV^{\bullet+}$. The reaction between the $(DPPy)Fe^{II}$ and O_2^- generate the Fe^{III}-(hydro)peroxo complex as catalytic intermediate (step 3), which either reacts with the substrate radical cation or undergoes oxygen atom transfer, forming the aldehyde and diol products (Figure 11).

Therefore, MV^{2+} acts as an electron shuttle to oxidize the $^*\mathbf{PS_{Ru}}$ to $[Ru^{III}(bpy)_3]^{3+}$ forming the one-electron reduced $MV^{\bullet+}$ radical, which can further reduce Fe^{III} complex to Fe^{II} form and O_2 to O_2^-. Then, the Fe^{II} complex reacts with O_2^- producing the iron(III)-peroxo species (step 3). At the same time, the oxidant $[Ru^{III}(bpy)_3]^{3+}$ regenerates back to the $\mathbf{PS_{Ru}}$ while oxidizing the substrate alkene into its radical cation. Finally, the alkene and the radical cation are oxidized by the Fe(III)-peroxo species, leading to the formation of two oxygenated compounds, the aldehyde, and the diol, closing the catalytic cycle. This complex mechanistic picture of the catalytic cycle was elucidated *via* systematic analysis by transient absorption spectroscopy of each step, which elucidated the role of the MV^{2+} in the formation of O_2^- and its role in the reduction of the Fe^{III} complex, giving the oxygen atom transfer reactive species Fe^{III}-(hydro)peroxo complex.

The influence of counter ion in the Ru polypyridyl complexes on the photoredox catalytic reactions has been underestimated. The group of Yoon proposed that the counter ion structure has a dramatic impact on the rate of [4+2] radical cation Diels–Alder cycloaddition reactions between electron-rich styrene and various dienes (Figure 13).[73] To prove the role of the anion in the photoredox process the $[Ru(bftmb)_3]^+$ (btfmb = 4,4′-bis(trifluoromethyl)-2,2′-bipyridyl) was studied with three different counter ions: aryl sulfonate (the most coordinating), PF_6^- (intermediate) and $Bar^F{}_4^-$ (the least coordinating). The photocatalyst with $Bar^F{}_4^-$ yielded a more powerful triplet excited state oxidant and longer radical chain length, resulting in the cycloaddition reaction complete in less than 20-minute, where the aryl sulfonate counterpart takes 24 h to achieve 14 % yield. The Stern-Volmer analysis proved that the bimolecular electron transfer rate constant (K_q) between $BAr^F{}_4^-$ complex and the styrene is two orders of magnitude higher than the aryl sulfonate complex in line with its superior activity. The K_q values were rationalized by a Coulombic ion-pairing interaction between the counter ion of the cationic photocatalyst and the substrate radical cation intermediate in the excited-state.

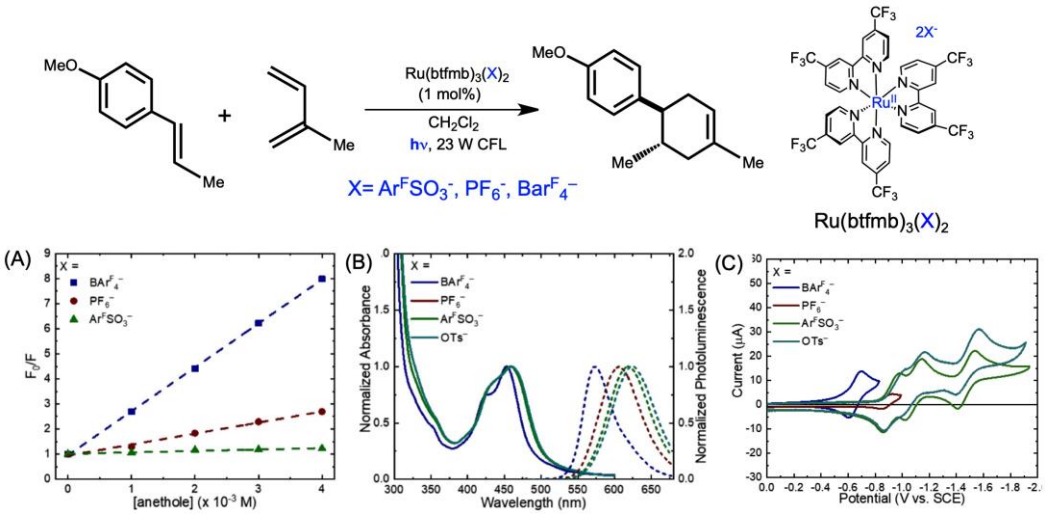

Figure 13: The scheme showing the radical cation Diels−Alder cycloaddition. (A) The Stern−Volmer plots for excited-state quenching of catalyst $Ru(btfmb)_3$ $(X)_2$ with three different counter ion, (B) its respective absorption and emission spectra, and (C) cyclic voltammogram at a scan rate of 100 mV/sec and in CH_2Cl_2 with 0.1 M electrolyte solution composed of the n-Bu_4N^+ salt of the indicated counterion. Reproduced with permission from ref.[73]

Further, photoluminescence spectra of $BAr^F{}_4^-$ the complex was blue-shifted by *ca.* 52 nm to the most coordinating tosyl complex. Consequently, the counter ion can alter the triplet excited state energy of the photocatalyst, influencing the Diels-Alder reactions. Finally, they have improved the catalysis with the least performing Ru complex with aryl sulfonate counterion to the level of the most performing $Ru(btfmb)_3$ $(BAr^F{}_4^-)_2$ complex by disrupting anion interaction with the cationic ruthenium complex with thiophosphotriamide as anion binding.

2.2 Reductive photoredox catalytic transformations mediated by $[Ru^{II}(bpy)_3]^{2+}$

The photocatalytic reductive transformation of organic molecules by $[Ru(bpy)_3]^{2+}$ (**PS_{Ru}**) photocatalyst has been extensively reported.[7,21] However, the mechanistic elucidation of their catalytic cycle by optical spectroscopic techniques are limited and mainly based on luminescence quenching studies. In 2006, the Garcia group reported Meerwein–Ponndorf–Verley reduction of carbonyl compounds to alcohols by employing **PS_{Ru}** as a photocatalyst, MV^{2+} as electron relay and triethanolamine as a sacrificial electron donor in isopropanol or ionic liquids (Figure 14).[74] The catalytic cycle follows via the reduction of MV^{2+} by $*[Ru^{II}(bpy)_3]^{2+}$ (***PS_{Ru}**) forming singly reduced $MV^{\bullet+}$ and $[Ru^{III}(bpy)_3]^{3+}$. In the presence of isopropanol, $MV^{\bullet+}$ forms MVH via hydrogen atom transfer. Then, the reduction of carbonyls is produced by the hydride transfer from MVH to form the alcohol products (Figure 14.A). The catalytic cycle is closed after the one-electron reduction of $[Ru^{III}(bpy)_3]^{3+}$ by TEOA to regenerate **PS_{Ru}**.

Laser flash photolysis was mainly employed to gather information about the mechanistic details. Laser excitation at 532 nm formed the ***PS$_{Ru}$** as judged by the differential absorption spectra (τ = 0.5 μs) and their spectral evolution in 8 μs; where a positive band at 350 nm and a negative band at 420 nm (disappearance of **PS$_{Ru}$**) is formed and vanished with the same kinetic trace (Figure 14.B, inset). In addition, the broad negative band in the 600-700 nm region is attributed to the emission of the ***PS$_{Ru}$**. The introduction of MV^{2+} resulted in the single electron transfer from ***PS$_{Ru}$** to MV^{2+} to form $MV^{\bullet+}$, as observed from the characteristic positive bands around 380 and 600 nm that last more than 150 μs (Figure 14.B, C). The hydrogen atom transfer from the solvent isopropanol to $MV^{\bullet+}$ was proposed based on the appearance of a new transient band around 500 nm, which resembles the *in-situ* generated MVH^+ by the reduction of MV^{2+} with $NaBH_4$ in acetonitrile (Figure 14.D).

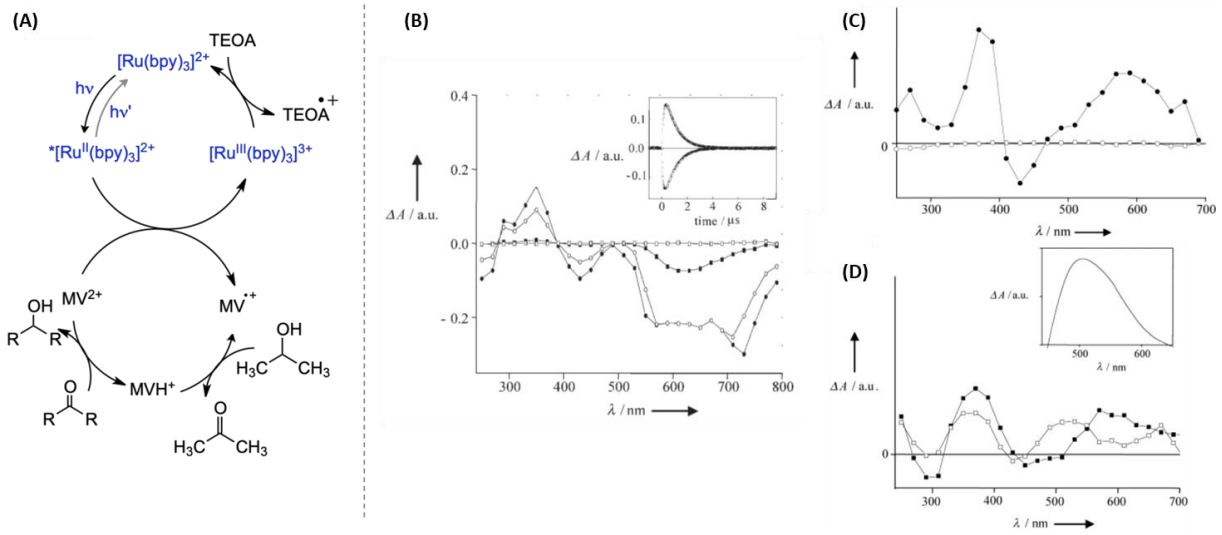

Figure 14: (A) Photocatalytic cycle showing the Meerwein–Ponndorf–Verley reduction of carbonyls by isopropanol. (B) TAS of **PS$_{Ru}$** in bmim-BF_4 at 0.5 (●), 1 (○), 3 (■) and 8 (□) μs after laser excitation at 532 nm. (Inset) Time profiles recorded at 350 (cycles) and 420 nm (triangles). (C) TAS of $[Ru^{II}(bpy)_3]^{2+}$ (under Ar) in the presence (●) and absence (○) of MV^{2+} recorded at 150 μs after 532 nm laser excitation. (D) TAS of a $[Ru^{II}(bpy)_3]^{2+}$/ MV^{2+} mixture in the absence (●) and presence of isopropanol (○). (Inset) The transient differential absorption spectrum of chemically generated MVH^+ by the reduction of MV^{2+} with $NaBH_4$ in acetonitrile. Adapted from the ref.[74]

PS$_{Ru}$ has been used in a myriad of organic transformation since the 1980s,[39] mainly by employing its direct photophysics.[7,8,21] However, in catalytic photoredox cycles, the photosensitizers (PS) evolve through different oxidation states, such as the PS^n reduced form (PS^{n-1}) or the oxidized form (PS^{n+1}), with their photophysics and photochemistry which is still barely explored. The photoexcitation of PS intermediates within the photoredox cycle opens new opportunities in photoredox transformations.[25] An illustrative example of its potential has been presented Goez et al.[75] They achieved the photoexcitation of

$[Ru(bpy)_2(bpy^{\bullet-})]^+$ ($\mathbf{PS_{Ru}}^{\bullet-}$) using a high-power (760 mJ cm^{-2}) laser source of irradiation at 532 nm and explored its reactivity.

$\mathbf{PS_{Ru}}^{\bullet-}$ is in-situ generated following the reductive quenching of ^{3}MLCT *$\mathbf{PS_{Ru}}$ excited state by ascorbate dianion (Asc^{2-}). In turn, the following photoexcitation of $\mathbf{PS_{Ru}}^{\bullet-}$ yields the formation of hydrated electrons ($e_{aq}^{\bullet-}$) and the recovery of the $\mathbf{PS_{Ru}}$ in its ground state (Figure 15). Under the experimental conditions employed, the $e_{aq}^{\bullet-}$ had a lifetime of 162 ns (Decay rate, K= $6.1 \bullet 10^6$ s^{-1}), long enough to be utilized in productive organic transformations (Figure 16.A-B). Nevertheless, the lifetime of the $e_{aq}^{\bullet-}$ is sensitive to the light intensity, concentration of the Asc^{2-}, $\mathbf{PS_{Ru}}$ and $AscH^-$ (Figure 16.C). The very high reduction potential of $e_{aq}^{\bullet-}$, *ca.* 2.9 V together with their natural lifetime in water makes the process viable to promote challenging reductive chemistry.[75]

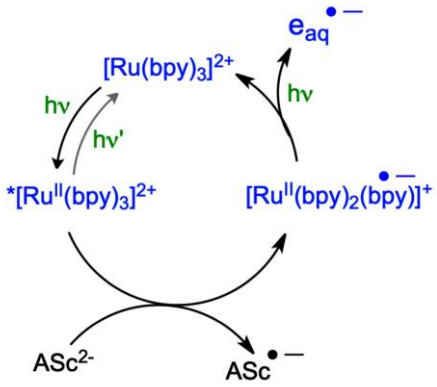

Figure 15: The photocatalytic cycle depicted shows the mechanism of photoionization of $\mathbf{PS_{Ru}}$ by two-pulse laser flash photolysis.

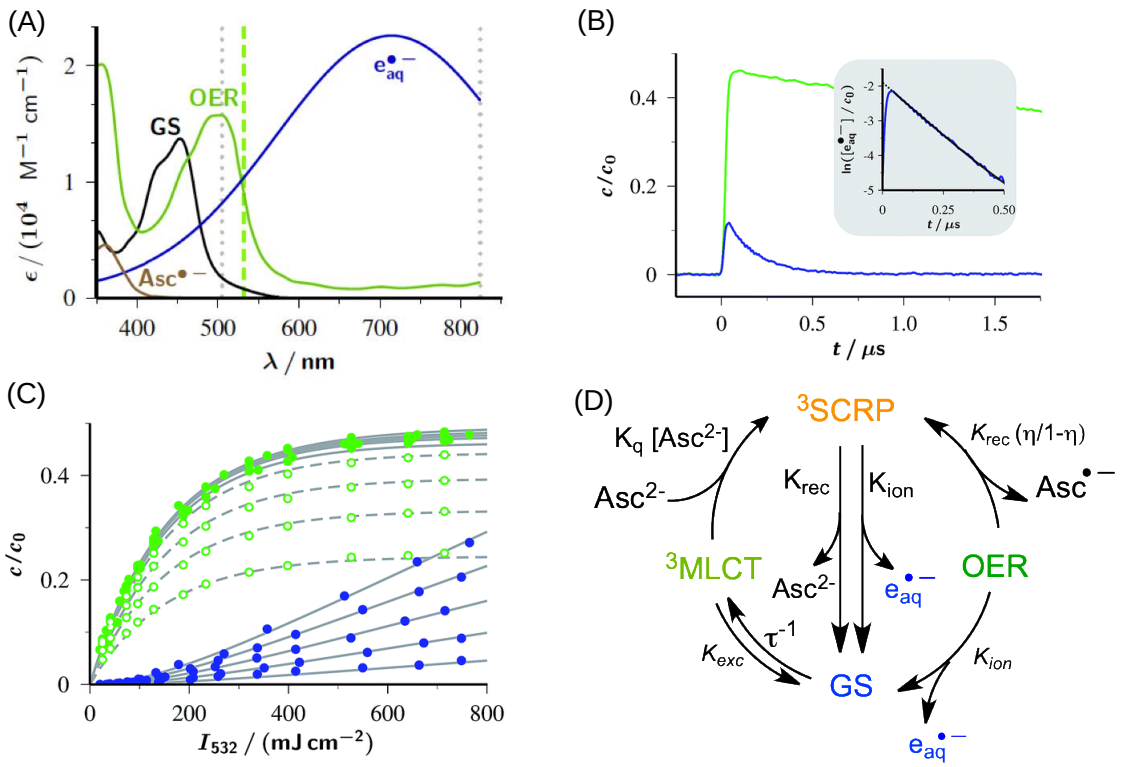

Figure 16: (A): The absorption spectra of components in the catalytic mixture, $\mathbf{PS_{Ru}}$ (GS), $\mathbf{PS_{Ru}^{\bullet-}}$ (OER), $Asc^{\bullet-}$ and $e_{aq}^{\bullet-}$.[76,77,78] Wavelengths to monitor OER and $e_{aq}^{\bullet-}$ (Dotted grey lines); Laser excitation wavelength (dashed green line). (B) Decay traces of OER (green) and $e_{aq}^{\bullet-}$ (blue) in the catalytic mixture (532 nm, 760 mJ cm^{-2}). Inset: first-order log-linear plot of $e_{aq}^{\bullet-}$. (C) Response of the catalytic system to the laser intensity and the sacrificial donor concentration. (D) Proposed mechanism, ^{3}SCRP is the spin-correlated radical pair ^{3}OER $Asc^{\bullet-}$. Reproduced with permission from ref.[75]

Kinetic studies and global analysis were used to study the full catalytic process (Figure 16.D). Interestingly, an intermediate form by a radical pair [^{3}OER-$Asc^{\bullet-}$] (^{3}SCRP) is produced during the quenching step. This radical pair is proposed to exist in the triplet state, which evolves and gives OER and $ASc^{\bullet-}$. The radical pair has an important consequence in the single flash generation of $e_{aq}^{\bullet-}$. If the radical pair is short-lived than the laser pulse, the catalyst cycle becomes the same as Figure 15. However, if the radical pair is long-lived than the laser pulse, ^{3}SCRP could be the channel to form the $e_{aq}^{\bullet-}$ without the need for forming reduced $\mathbf{PS_{Ru}}$ (Figure 16.D). The same group also developed several strategies to improve and control the generation of $e_{aq}^{\bullet-}$ from $\mathbf{PS_{Ru}}$, utilizing tandem energy/electron transfer processes on micellar interphase;[76] with low power LED or even sunlight for promoting the generation of $e_{aq}^{\bullet-}$.[78,79] These strategies have been applied to catalytic transformations of alkyl or aryl halides and aromatic ketones.

2.3 $[Ru(bpy)_3]^{2+}$ energy transfer mediated photocatalysis

As explained above, Ru polypyridyl complexes are suitable for photoinduced energy transfer (PEnT), but are still poorly developed in photocatalysis.[49] Nevertheless, there are interesting examples, such as the one reported by the Yoon group in 2016. They studied the enantioselective cycloaddition reactions of 2-hydroxychalcones with dienes to form vinyl cyclobutanes by the energy transfer mechanism from the $[Ru(bpy)_3]^{2+*}$ excited state.[80] To note, the energy of the $[Ru(bpy)_3]^{2+*}$ triplet excited state is too low ($E_{T(PSRu)}$= 45 kcal/mol) for developing many synthetic applications, like in the case described. However, the addition of a Lewis acid ($Sc(OTf)_3$) significantly lowers the triplet energy of substrate 2-hydroxychalcones. The excited state emission spectra of hydroxychalcone showed that the triplet energy is 54 kcal/mol. The addition $Sc(OTf)_3$ to hydroxychalcone solution from a Sc-hydroxychalcone adduct formed the emission around 876 nm, with a correspondnig triplet energy of 33 kcal/mol. Therefore, reaction changes from endergonic to exergonic by the addition of $Sc(OTf)_3$.

Similarly, Batch and Wenger's groups reported another example of productive triplet-triplet energy transfer from Ru(II) complexes. They showed that it could be utilized for the enantioselective synthesis of cyclobutanecarbaldehydes by a [2+2] photocycloaddition reaction.[81] The excited state Ru(II) complex undergoes PEnT to preformed chiral eniminium salts, which follows the cycloaddition with olefins and finally hydrolyses to give the chiral cyclobutanecarbaldehyde product. They have employed laser flash photolysis to show that the reaction operates through both electron and energy transfer pathways. Further spectroscopic studies demonstrated that, although both PET and PEnT occur from Ru(II) complexes as competing events, only energy transfer generates the reaction intermediate, intercepted by an olefin towards cycloaddition reactions.

The group of Miyake reported the use of energy transfer to activate photoredox dual catalysis of C-N crosscoupling reactions. In this case, the $\mathbf{PS_{Ru}}$ acts as an energy donor and a Ni(II) salt ($[Ni(II)Br_2(amine)_x]$) as an energy acceptor.[82] Actually, Ni(II) salts can be directly excited, producing SET processes without adding photocatalysts to produce C-N cross-coupling products.[82] The detailed mechanistic studies proved the involvement of Förster energy transfer from $[Ru(bpy)_3]^{2+*}$ to an *in-situ* formed Ni-amine complex. Interestingly, in this case, a SET process between $[Ru(bpy)_3]^{2+*}$ and the Ni-amine complex is thermodynamically not feasible.

3. Iridium polypyridyl complexes: $[Ir(ppy)_3]$ and $[Ir(ppy)_2bpy]^+$ and its analogues

Although $[Ru(bpy)_3]^{+*}$ type photosensitizers have excelled in catalytic applications, they also have limitations in their photochemical and redox properties, limiting the tuning of the redox potential. In contrast, d^6 Ir cyclometallated polypyridyl complexes, such as $[Ir(C^N)_3]$ and $[Ir(C^N)_2N^N]^+$ (where C^N= 2-phenyl pyridine, ppy and N^N= bipyridine, bpy),[83,84,85,86] have extraordinary flexibility in terms of modulation of the coordination sphere and remarkable photochemical properties (Figure 17). In fact, d^6-Ir cyclometallated polypyridyl complexes have emerged as photoredox catalysts with broad applicability in synthetic organic methodology.

The photochemical properties of Ir(III) complexes can be rationalized by considering the highest-occupied and lowest-unoccupied molecular orbitals (HOMO and LUMO, respectively). In the case of neutral homoleptic Ir(III) complexes like *fac*-$(Ir(ppy)_3)$, the HOMO is delocalized between the t_2g orbital of the Ir atom and the π-orbital system of 2-phenylpyridinate ligand, while the LUMO is mainly located on the π^*-orbitals of the 2-phenylpyridinate.[87] However, in the case of heteroleptic complexes, like $[(Ir(ppy)_2bpy]^+$, the LUMO is located on bipyridine ligand.

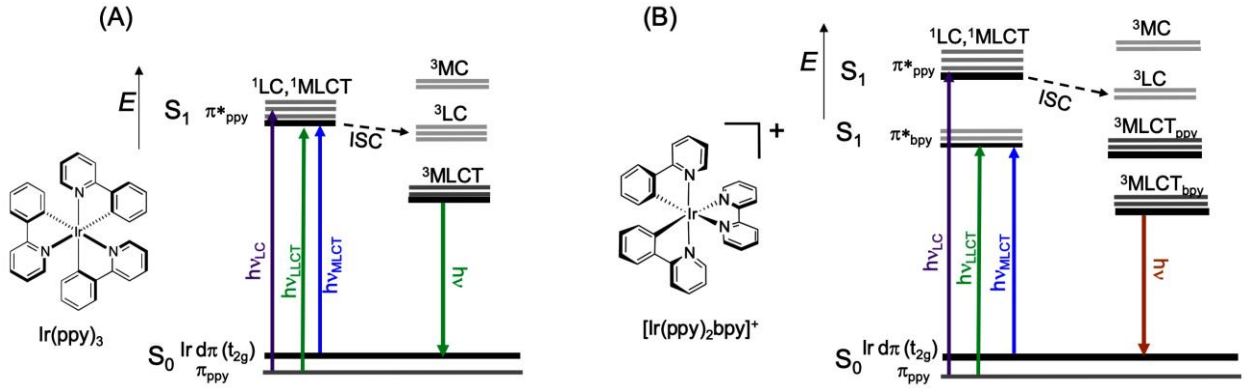

Figure 17: (A) Jablonsky diagram showing the excited state relaxation pathway of Ir(III) complexes of (A) *fac*-$(Ir(ppy)_3)$ and (B) $[Ir(ppy)_2bpy]^+$.

The photoexcitation of the *fac*-$(Ir(ppy)_3)$ complex populates ^{1}LC and ^{1}MLCT transition states, depending on the energy of the irradiated light. These two electronic states are usually coupled together as they have common LUMO located on the cyclometallated ppy ligand. Nevertheless, the internal conversion from ^{1}LC to ^{1}MLCT occurs in the fs timescale. Since MLCT transition states have a strong spin-orbit coupling interaction with the Ir(III) centre, the intersystem crossing from $^1MLCT_{ppy}$ to $^3MLCT_{ppy}$ is highly efficient (quantum yield ~1).[88] However, in the case of $[(Ir(ppy)_2bpy]^+$, the ^{1}MLCT intersystem crossing is more complex, and the emission involves a low lying triplet manifold. The intersystem crossing transitions follow in the order ^{3}LC, $^3MLCT_{ppy}$ and $^3MLCT_{bpy}$, according to their energy level. Then, the

emission from heteroleptic complexes is best described as a linear combination of the emission from the ^{3}LC and ^{3}MLCT states.[87]

fac-(Ir(ppy)$_3$) presents an absorption spectrum with high excitation energy bands below < 300 nm (^{1}LC bands) with a peak around 390 nm, assigned to ^{1}MLCT transition, and spectral bands between 450-500 nm corresponding to forbidden ^{3}MLCT bands (Figure 18). Nevertheless, since the energy states in Ir(III) complexes are highly mixed due to spin-orbit coupling, these bands are imprecisely assigned by TD-DFT calculations.[89,90] The emission spectrum shows a broad featureless band with a peak at around 540 nm (^{3}MLCT transition).[87]

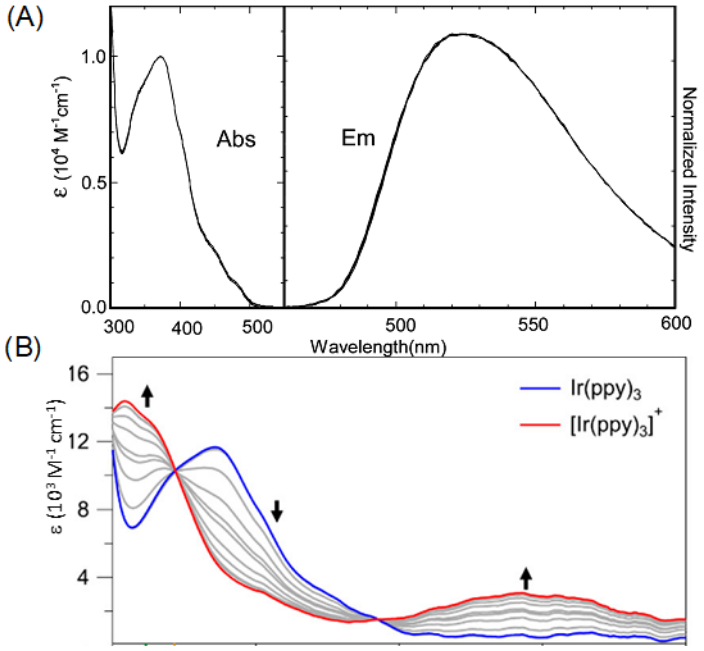

Figure 18: (A) Absorption and emission spectra of *fac*-(Ir(ppy)$_3$) in acetonitrile.[89] (B) The absorption spectra showing the oxidation of *fac*-(Ir(ppy)$_3$) (blue) to *fac*-[Ir(ppy)$_3$]$^+$ (red) by UV-Vis spectroelectrochemistry. Reproduced with permission from ref.[91]

In 2012, Stephenson *et al.* employed cyclometallated Ir(III) complexes as photocatalysts for the reductive dehalogenation of unactivated aryl, alkyl and alkenyl iodides, as well as intramolecular cyclizations in the presence of electron donors like tributylamine, Hantzch ester, or formic acid.[92] In their studies, the biscyclometallated complex [Ir(ppy)$_2$(dtbbpy)]PF$_6$ was able to reduce only activated carbon-halogen bonds, whereas *fac*-(Ir(ppy)$_3$), the more reducing complex, was able to reduce also unactivated substrates. The reducing nature of *fac*-(Ir(ppy)$_3$) was attributed to the three potent electron-donating cyclometallated 2-phenylpyridine ligands.[92] Although no spectroscopic studies were performed to elucidate the mechanism, it was proposed that the catalytic cycle starts with the oxidative quenching of

the *fac*-($Ir(ppy)_3$) with the alkyl iodide to form the one-electron oxidized Ir(IV) intermediate, and the reductive cleavage of the alkyl iodide to generate a carbon-centred radical. Then, the carbon-centred radical could proceed *via* radical cyclization or hydrogen atom abstraction from tributylamine, Hantzsch ester, or formate. The photocatalyst regenerates the ground state by oxidation with electron donors like tributylamine, Hantzsch ester, or formate. Recently, the spectroscopic evidence of the ($[Ir^{IV}(ppy)_3]^+$) intermediate, formed in the oxidative quenching, was proposed by spectroelectrochemistry studies.[91] As evident in Figure 18.B, Ir(IV) shows a broad absorption band > 500 nm and a higher energy transition band around 320 nm. The electrochemical oxidation was fully reversible with clear isosbestic points 346 and 486 nm, implying the formation of $[Ir(ppy)_3]^+$.[91] The formation of the reduced form of ($Ir(ppy)_3$) in reductive quenching is highly unlikely since it is more reducing than the amine-based sacrificial donors ($E_{1/2}(Ir^{IV/*III}) = -1.73$ V, $E_{1/2}(Ir^{III*/II}) = 0.31$, $E_{1/2}(NR_3^{+/0}) = 0.8 - 1.0$ V *vs*. SCE).

Although the *fac*-($Ir(ppy)_3$), $[Ir(ppy)_2(bpy)]PF_6$ complexes and its derivatives have been widely applied as a photocatalyst due to their strong reducing nature, it remains challenging to use them directly for the dehalogenation of unactivated alkyl bromides or chloride, by following conventional photoredox cycles.[89] Certainly, stable carbon–chlorine bonds are beyond the energetic limit of a conventional outer-sphere single electron transfer mechanisms. However, in the case of excitation of their reduced state (Ir(II)), like ruthenium polypyridine photosentitizers,[76,93,94,79,95,96] the redox power could be reducing enough. In this regard, Kunz and König's group have explored in an aqueous solution the potential use of $[Ir(dtbby)(ppy)_2]$ compartmentalized in micelles.[97] Under these conditions, it is proposed that the one-electron reduced $[Ir(dtbby)^{\bullet-}(ppy)_2]$ could be excited by blue photons and then eject an electron. The compartmentalization in a microheterogeneous environment helps to maintain the $PS^{\bullet-}$ isolated from the rest of the solution, prolonging the back-electron kinetics and therefore permitting the organic reactivity. The catalytic system was optimized for the activation of alkyl chlorides and applied to challenging inter- and intra-reductive cyclization reactions.

The group of Wenger reported the strong photoreductant and water-soluble sulfonated iridium complex **Irsppy** (Figure 19). **Irsppy** promoted the dehalogenation of chloroacetates to acetates and trifluoromethyl to difluoromethyl.[95] The mechanism of action is proposed to follow the formation of a hydrated electron by a two-pulse excitation process (430 and 532 nm). The laser pulse at 430 nm first generates a ^{3}MLCT excited state, presumably after fast relaxation from higher energy ^{1}MLCT levels. The transient absorption spectrum, corrected for the emission, shows a positive transient band at wavelength values lower than 400 nm and a band centred *ca.* 510 nm (Figure 19.C). The excitation features the ^{3}**Irsppy**

excited state has a lifetime decay (τ) of 1.6 μs. If a second laser pulse is applied at 532 nm once the ^{3}**Irsppy** is fully formed (after a delay time of 450 ns), the ^{3}**Irsppy** (^{3}MLCT excited state) is photoionized, giving a hydrated electron ($e_{aq}^{\bullet-}$) and the **Irsppy**$^{\bullet+}$ radical cation (Figure 19.D). Finally, the **Irsppy**$^{\bullet+}$ regenerates back to its ground state upon reduction by common sacrificial electron donors.

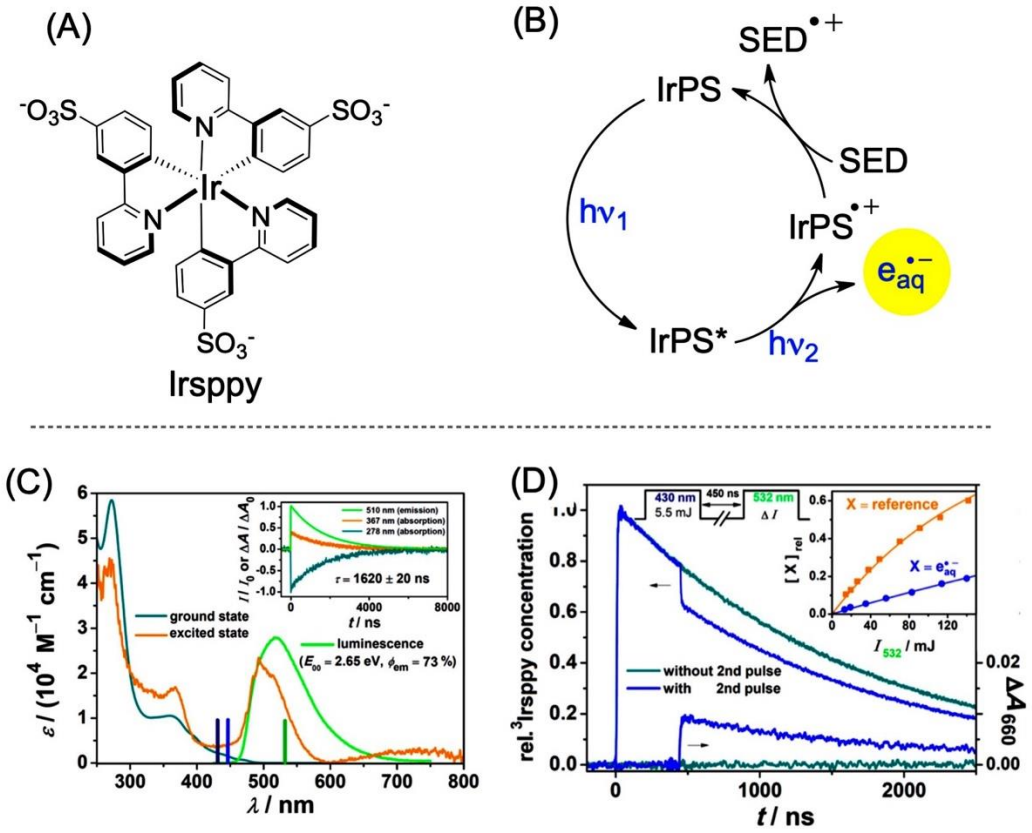

Figure 19: (A) Line drawing of the sulfonated photocatalyst (**Irsppy**), and (B) the catalytic cycle proposed showing the generation of $e_{aq}^{\bullet-}$ followed by the regeneration after reductive electron transfer from a suitable sacrificial electron donor (SED). (C) Ground-state absorption, emission, and excited-state absorption of **Irsppy**. Vertical lines show the wavelengths used for the excitation (laser flash photolysis, 430 and 532 nm; and preparative photolysis experiment, 447 nm). Inset: Kinetic traces upon excitation with 430 nm laser pulses (5 mJ).[95] (D) Kinetic decay of excited **^{3}Irsppy** (upper traces, left y-axis) and $e_{aq}^{\bullet-}$ (lower trace right y-axis) after the two-pulse excitation synchronized at 450 ns delay time (scheme on the top of decay trace), where the cyan line corresponds to the blank decay after one laser alone. (Inset) Excited **Irsppy** bleaching/$e_{aq}^{\bullet-}$ formation (blue) at different light intensities of the second laser, compared with the reference reaction of $[Ru(bpy)_3]^{2+}$ excitation (orange), both relative to the initial concentration of the respective signal precursor. $[Ru(bpy)_3]^{2+}$ is used as an actinometer. Reproduced with permission from ref. [95]

Additional subtraction of transient absorption spectrum after two pulse excitations with the spectrum obtained by monophotonic excitation gave the absorption spectrum of a hydrated electron.[76,77,78] The kinetics and associated spectra were assigned to the formation $e_{aq}^{\bullet-}$, in line with

previous reports, and further quenching experiments with chloroacetate. Finally, this new methodology reported for **Irsppy** was applied to the dehalogenation reaction of organochlorides and organofluorides.

Heteroleptic Ir(III) polypyridyl complexes, such as $[Ir(C^N)_2(N^N)]^+$, have also been broadly used as photoredox catalysts due to their straightforward redox tunability by independent ligand modification on either C^N or N^N ligands. Among others, the group of Bernhard and Malliaras have developed a series of cationic heteroleptic iridium complexes by modifying either C^N or N^N ligands (Figure 20).[83,84,98,40] From these studies, it was proposed that the HOMO in $[Ir(C^N)_2(N^N)]^+$ type complexes are mainly delocalized between the Ir metal centre and the cyclometalated C^N ligands, while the LUMO lies on the N^N ligand. Therefore, a substitution of the cyclometalated C^N ligand with an electron-withdrawing group stabilizes the HOMO and increases the oxidation potential. Whereas the introduction of an electron donating group at the N^N ligand (LUMO) increases the reductive character (Table 3).

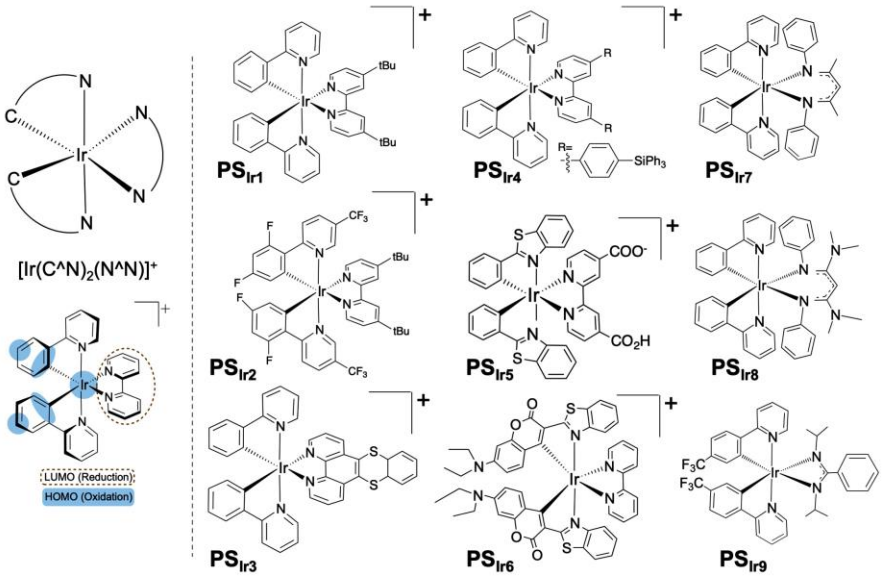

Figure 20: The heteroleptic $Ir(C^N)_2(N^N)]^+$ complexes with various substitution over the C^N and N^N ligands, which is generally used in photoredox catalysis.

Table 3: Photophysical and photoredox properties of heteroleptic Ir(III) complexes, $\mathbf{PS_{Ir1}}$-$\mathbf{PS_{Ir9}}$.[99]

	τ (μs)	E_{T1} (eV)	E^{ox} (V)	E^{red} (V)	$*E^{ox}$ (V)	$*E^{red}$ (V)	ref.
$\mathbf{PS_{Ir1}}$	0.60	2.17	0.81	−1.61	−1.36	0.26	[100,101,102]
$\mathbf{PS_{Ir2}}$	2.3	2.58	1.29	−1.77	−1.61	0.49	[103,104,105]

PS_{Ir3}	47.1	2.13	0.91	−1.69	−1.22	0.52	[106]
PS_{Ir4}	0.47	2.34	0.71	−1.66	−1.63	0.71	[107]
PS_{Ir5}	0.099	2.38	0.80	−1.46	−1.58	0.80	[108]
PS_{Ir6}	0.081	2.13	0.70	−1.60	−1.43	0.53	[109]
PS_{Ir7}	0.20	2.4	−0.07	−2.4	−2.5	0.0	[110,111]
PS_{Ir8}	0.76	2.3	−0.26	−2.7	−2.6	−0.4	[111,110]
PS_{Ir9}	0.069	2.33	0.26	−2.29	−2.07	0.04	[112]

The UV/Vis absorption spectrum of $[Ir(ppy)_2bpy]^+$ is dominated by the LC transitions below 350 nm, and two MLCT transitions at 430 and 470 nm assigned to the ppy and bpy ligands, respectively (Figure 21).[83,84] The emission spectrum of $[Ir(ppy)_2bpy]^+$ in acetonitrile shows a broad band with a peak at 584 nm, assigned to $^3MLCT_{bpy}$ transitions. The reductive electron transfer from an electron donor like Et_3N generates its reduced form ($[Ir^{III}(ppy)_2(bpy^{\bullet-})]$, which exhibit absorption features from 200 to 527 nm and a broad band from 600 to 1100 nm. These broad absorption features are attributed to the $bpy^{\bullet-}$ of the complex, $([Ir^{III}(ppy)_2(bpy^{\bullet-})]^0$.[113,114] The cyclic voltammogram shows a reversible wave with the first reduction corresponding to the reduction of N^N-centered LUMO and the second wave refers the low-lying C^N π* orbital. The oxidation wave is quasi-reversible and involves the Ir^{III}/Ir^{IV} redox couple with a strong influence from the C^N ligand.[40]

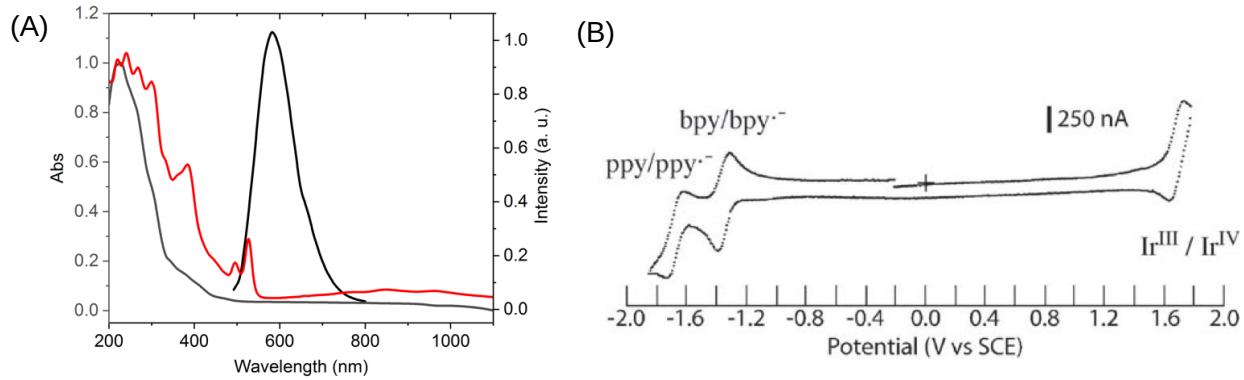

Figure 21: (A) The steady-state absorption (gray) and emission spectrum (black) of $[Ir(ppy)_2bpy]^+$ and the absorption spectrum of *in-situ* generated $[Ir(ppy)_2(bpy^{\bullet-})]^0$. (B) The cyclic voltammogram shows the redox behaviour of the Ir(III) complex. Reproduced from ref.[84]

Although $[Ir(ppy)_2bpy]^+$ has been widely used in photoredox applications, the understanding of the electron transfer dynamics is still under elaboration. Some of us have reported the mechanistic study of electron transfer (ET) from the *in-situ* formed $[Ir^{III}(ppy)_2(bpy^{\bullet-})]^0$ to Co(II)-based catalysts with electron-withdrawing and electron-donating substituents in the context of the water reduction reaction.[115,116] Steady-state and transient optical spectroscopic techniques were decisive to detect and study the elusive Co(I) intermediate generated. Besides, the mechanisms of photocatalytic transformations of organic compounds with $[Ir(ppy)_2bpy]^+$ generally relied on steady-state emission quenching and Stern-Volmer studies, redox values or the bond dissociation energy of the reaction components.

To address this shortcoming, the group of Nocera has performed mechanistic studies on each reaction step involved in the photoredox hydroamidation of olefins.[117] The reaction proceeds via the excitation of $[Ir(dF\text{-}CF_3\text{-}ppy)_2(bpy)]$, followed by a reductive electron transfer with 2-cyclohexen-1-yl(4-bromophenyl)carbamate (**1a**) to form $[Ir(dF\text{-}CF_3\text{-}ppy)_2(bpy^{\bullet-})]$ and the amidyl radical after proton-coupled electron transfer (PCET) with the base dibutylphosphate base, (Pi^{Bu2}, Figure 22).[118] After cyclization of the amidyl radical, alkyl thiol (2,4,6-Trimethylphenylthiol, MesSH) serves as a hydrogen atom donor to the cyclized radical intermediate to furnish the final carbamate product. The reaction yield was 86 % with a quantum efficiency of *ca.* 4.7 % (Quantum efficiency, Φ_p = total product formed/photons utilized) measured with the actinometer ferrioxalate (λ_{exc} = 380 nm). The Stern-Volmer quenching studies validate the thermodynamic feasibility of the reductive quenching of $*[Ir(dF\text{-}CF_3\text{-}ppy)_2(bpy)]$ by the substrate in the presence of base Pi^{Bu2}.

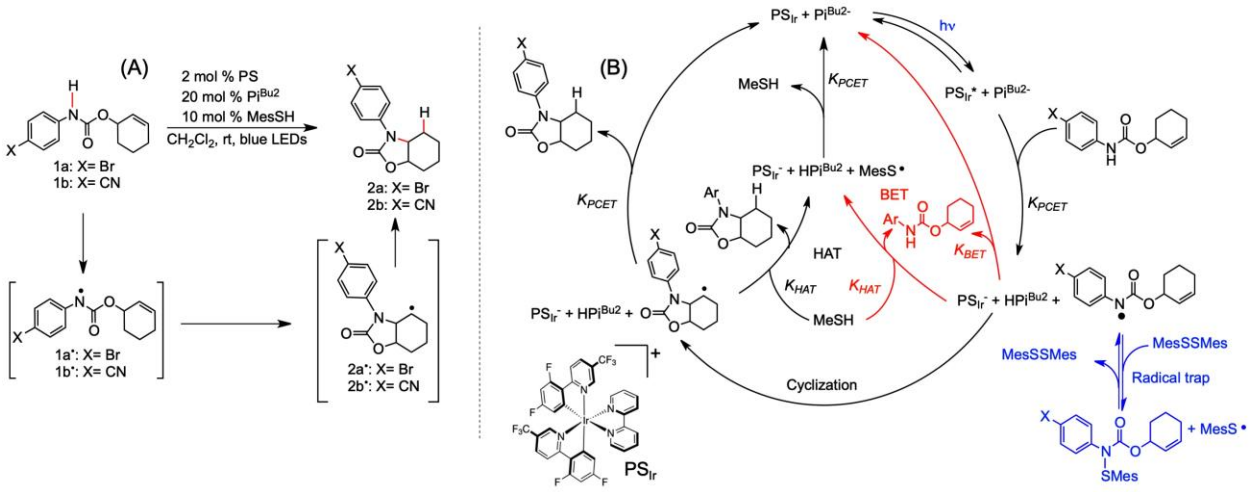

Figure 22: (A&B) Scheme of the photoredox hydroamidation of olefins and its photocatalytic cycle.

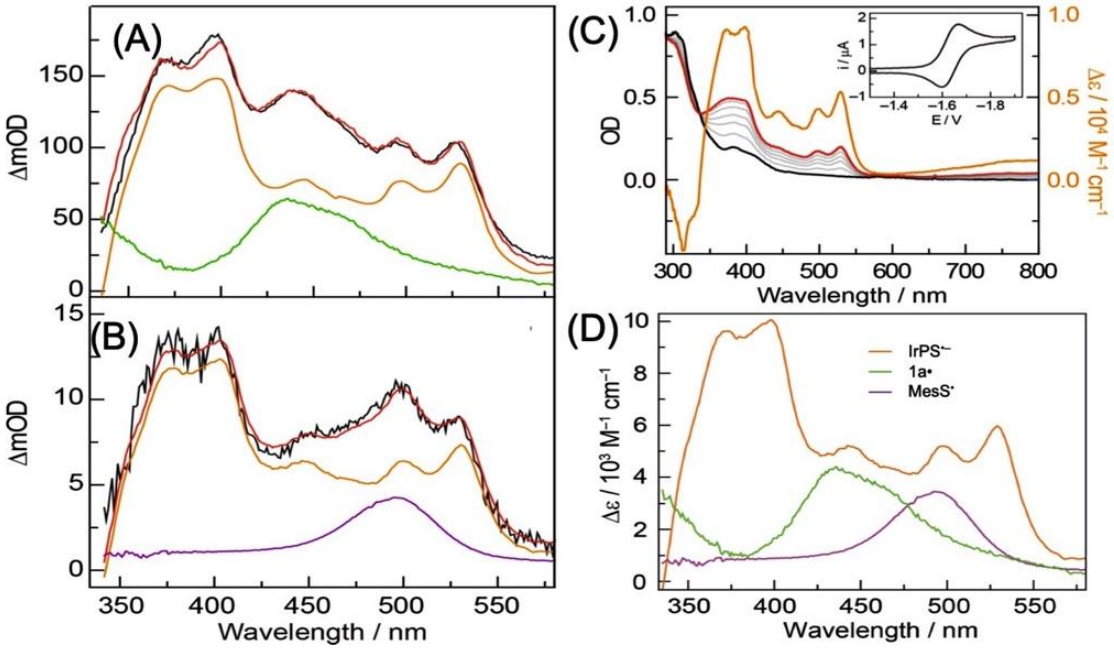

Figure 23: A) The transient absorption spectrum (TAS, black curve) of the catalytic mixture containing [Ir(dF-CF_3-ppy)$_2$(bpy)] (100 μM), Pi^{Bu2} (1 mM) and substrate **1a** (10 mM) after excitation with a blue laser (355 nm). The red trace was obtained by the mathematical addition of the spectrum of [Ir(dF-CF_3-ppy)$_2$(bpy)$^{\bullet-}$] (orange) and **1a$^\bullet$** (green trace). The TAS of **1a$^\bullet$** was generated separately from the camphorquinone (CQ) (10 mM), $PiBu_2$ (1 mM) and **1a** (10 mM) mixture. The transient absorption spectrum of [Ir(dF-CF_3-ppy)$_2$(bpy)$^{\bullet-}$] (orange curve) was obtained by subtracting the absorption spectrum of [Ir(dF-CF_3-ppy)$_2$(bpy)] from [Ir(dF-CF_3-ppy)$_2$(bpy)$^{\bullet-}$] in spectroelectrochemistry experiments (shown as C). (B) TAS of [Ir(dF-CF_3-ppy)$_2$(bpy)] (100 μM), MesSH (10 mM) and Pi^{Bu2} (1 mM) mixture (black curve) after photoexcitation at 440 nm. TAS of MesS• (purple curve) obtained after photolysis of the MesSSMes solution in CH_2Cl_2, the spectrum of [Ir(dF-CF_3-ppy)$_2$(bpy)$^{\bullet-}$] (orange) obtained in spectroelectrochemistry experiments (C) and the mathematical addition (red) of both orange and purple curve. (D) The spectra of key transient species that are part of the photocatalytic cycle and its extinction coefficients (Δε), [Ir(dF-CF_3-ppy)$_2$(bpy)$^{\bullet-}$], 1a$^\bullet$, MesS$^\bullet$. Reproduced with permission from ref. [117]

TAS studies have been used to identify the key reaction intermediates formed in the catalytic cyle; *[Ir(dF-CF_3-ppy)$_2$(bpy)], [Ir(dF-CF_3-ppy)$_2$(bpy$^{\bullet-}$)], amidyl radicals and thiol radicals (Figure 23).

TAS of the catalytic mixture containing [Ir(dF-CF_3-ppy)$_2$(bpy)], the substrate (**1a**, Figure 22) and the base (Pi^{Bu2}) measured after 2.5 μs of the laser pulse (λ_{exc} 355 nm), shows an absorption spectrum corresponding to a mixture containing both [Ir(dF-CF_3-ppy)$_2$(bpy$^{\bullet-}$)] and **1a$^\bullet$** (Figure 23.A). The absorption spectrum could be reproduced by generating IrPS$^{\bullet-}$ and **1a$^\bullet$** independently and further mathematical addition (black, Figure 23.A). The [Ir(dF-CF_3-ppy)$_2$(bpy$^{\bullet-}$)] absorption spectrum was generated by spectroelectrochemistry (black and red curve, Figure 23.C). Whereas the transient absorption spectrum of **1a$^\bullet$** was determined by a different light-induced reaction between **1a** and a radical initiator camphorquinone (CQ), as its excited-state CQ* is a good hydrogen atom abstractor (green curve, Figure

23.A). Similarly, the transient absorption spectra of the [Ir(dF-CF_3-ppy)$_2$(bpy)], MesSH and Pi^{Bu2} mixture shows the signature of the intermediate $MesS^{\bullet}$ confirming that [Ir(dF-CF_3-ppy)$_2$($bpy^{\bullet-}$)] can also be formed by reductive quenching with the thiol in the presence of a base (purple trace, Figure 23.B). However, $MesS^{\bullet}$ can also be formed in the catalytic mixture after amidyl radical cyclization via the HAT process. Finally, comparing all kinetic rates determined by transient spectroscopy, the back-electron transfer (BET) from the amidyl radical to [Ir(dF-CF_3-ppy)$_2$($bpy^{\bullet-}$)] and the HAT process with the alkyl thiol is found to slow the catalysis and reduce the quantum efficiency to 4.7 %. Nevertheless, the authors found a method to attenuate the BET process while trapping the amidyl radical with a disulfide trap and allowing the radical to be released at a later stage of the photoredox cycle, and finally boosting the catalysis by a factor of 4.

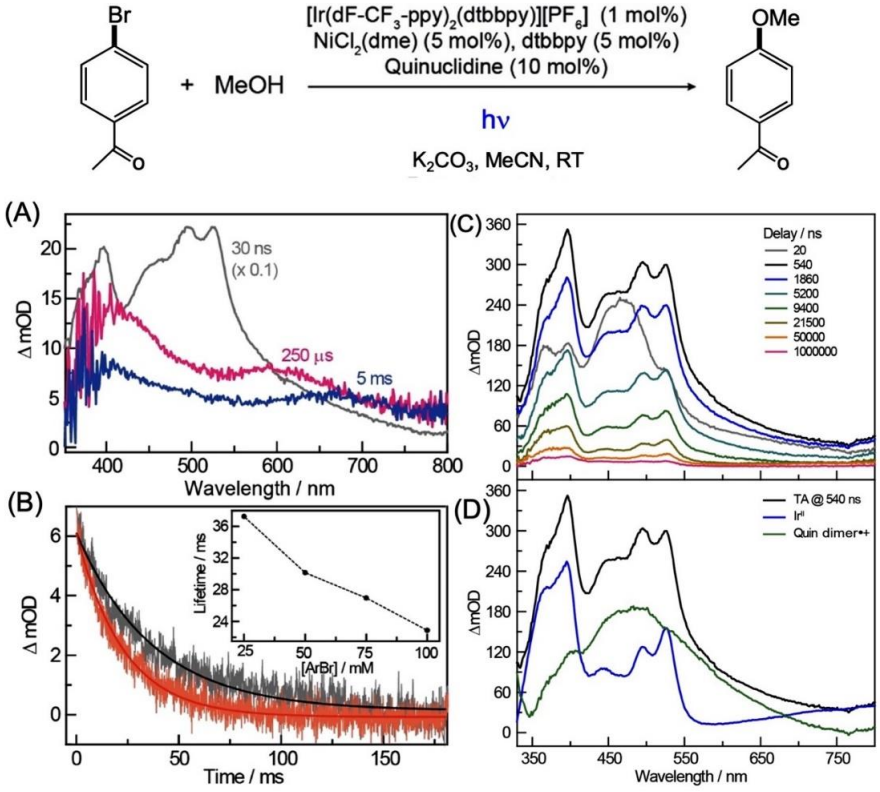

Figure 24: (A) TAS of the mixture containing [Ir(dF-CF_3-ppy)$_2$(dtbbpy)] (200 µM), $NiCl_2$(dme) (5 mM) and quinuclidine (50 mM) in CH_3CN, its transient absorption kinetics and the fits at 670 nm (B), monitored after the addition of 25 mM (gray) and 100 mM (orange) of 4'-bromoacetophenone (Inset: fitted lifetime in the presence of different concentrations of aryl bromide). (C) The evolution of TA spectra after the excitation of [Ir(dF-CF_3-ppy)$_2$(dtbbpy)] in the presence of quinuclidine and at different elapsed times after laser excitation. (D) The deconvoluted TA spectrum of the catalytic mixture at 540 ns when all Ir(III) excited states disappeared (black), the green curve shows the spectrum of transient intermediate (quinuclidine dimer radical cation) after subtracting [Ir(dF-CF_3-ppy)$_2$($bpy^{\bullet-}$)] contribution (blue, obtained by spectroelectrochemistry) from the TA spectrum of the catalytic mixture (black) Reproduced with permission from ref.[119]

Later, the same group has performed detailed mechanistic studies with laser spectroscopy to optimize the Ni-catalyzed photoredox transformation of aryl bromide into respective anisole (Figure 24).[119] The nanosecond TAS was used to investigate the different catalytic steps of the reaction. The TAS of the mixture containing $NiCl_2$(dme), dtbbpy, quinuclidine, and the Ir photocatalyst measured after 30 ns of the laser pulse shows the spectral signature of both ($[Ir(dF(CF_3)(ppy)_2(dtbbpy^{\bullet-})]PF_6$), and the quinuclidine dimer radical cation (Figure 24). After several hundreds of microseconds, the spectrum evolves to a new species with absorption features at 415 and 595 nm, which is further evolving into a new broad band centred around 670 nm after 5 milliseconds. Since these long lifetime spectral features were missing in the absence of the Ni(II) catalyst, they were attributed to the formation of low-valent Ni-species. The kinetics at 670 nm was found to be quenched by the addition of 4'-bromoacetophenone (Figure 24.B). To rationalize these spectral features, the authors monitored the catalytic reaction sequence spectroscopically under LED irradiation. The spectral features of the catalytic reaction mixture were also in agreement with the emergence of a new absorption peak around 670 nm. Finally, to assess the Ni(II) reduction product as the catalytic intermediate, the Ni (I) species was synthesized and characterized by X-ray diffraction studies and proved the presence of a Ni(I/II) dimer in equilibrium with the Ni(I) catalytically active species. Then the experimental absorption features assigned to the low valent Ni species formed during the catalysis were also matched with the computational DFT studies. As a learned lesson, the attenuation of the concentration of Ni(I) intermediate with low photon flux irradiation is found to hamper the deleterious dimer formation and finally boosting the catalysis by a factor of 15.

3.1 Ir(III) complexes in energy transfer mediated photocatalysis

Like in Ru(II) polypyridyl complexes, the photocatalysis mediated by energy transfer from Ir(III) complexes presented in this section can also be used to trigger organic transformations. The group of MacMillan and McCusker have demonstrated the role of a triplet energy transfer from $[Ir(ppy)_3]$ to dtbbpy•Ni(0) complex (dtbbpy is 4,4'-di-tertbutyl-2,2'-bipyridine) in a cross-coupling catalyzed reaction.[120]

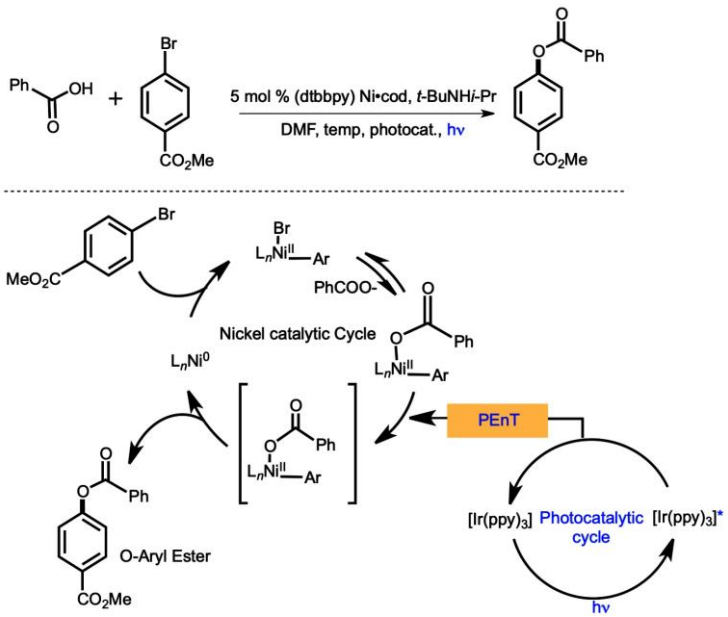

Figure 25: The photocatalytic reaction and its mechanism for the nickel-catalyzed coupling of aryl halides with carboxylic acids via the excited state of Ni(II) adduct, formed after the energy transfer from the photoexcited $Ir(ppy)_3$.

The reaction starts with the oxidative addition of an aryl halide to a low valent Ni (0) complex to form an aryl–Ni(II) species (Figure 25). The subsequent coordination of benzoate forms an aryl-Ni(II)-carboxylate complex, which is photoactivable by triplet energy transfer from Ir(III) complex. Finally, O-aryl ester product is formed by the reductive elimination from the excited state of aryl–Ni(II)-carboxylate adduct. Stern-Volmer luminescence quenching studies demonstrate that PEnT from the $\mathbf{PS_{Ir}}$ induces C-O reductive elimination from the Ni(II) adduct.

Later the group of Glorius and Guldi also utilized the energy transfer photosensitization of disulfides by Ir(III) photocatalyst towards hydroalkyl/aryl thiolation of alkenes.[121] The triplet energy of the photocatalyst, $[Ir(dF(CF_3)ppy)_2(dtbbpy)](PF_6)$ ($dF(CF_3)ppy$ = 2-(2,4-difluorophenyl)-3-trifluoromethylpyridine, dtbbpy = 4,4′ -di-tert-butyl-2,2′ -bipyridine), match with the dimethyl disulfide to produce an effective Dexter energy transfer, and to afford dimethyl thienyl radical as a catalytic intermediate for the anti-Markonikov addition to alkene. The Stern Volmer analysis and consequent ns-TAS experiments proved the phosphorescence quenching of $\mathbf{PS_{Ir}}$ complex by alkyl thiols followed by the adduct formation between the excited donor and acceptor, resulting in the homolytic cleavage of S-S bond and the corresponding thienyl radical.

4. Heterogenized Ru and Ir complexes for photoredox applications

Ru or Ir-based metal complexes and metal-free organic dyes have been at the forefront of homogenous photoredox catalysis, and their heterogenization is growing in attention.[122] Here, there are included some examples of RuPS, or IrPS anchored on heterogenous materials like TiO_2,[123] SiO_2,[124] zeolites,[125] metal-organic-frameworks (MOF),[126,127] together with selected examples of photoinduced organic transformation.

The advantages of heterogenizing molecular photocatalysts are their easy separation from the crude mixture of reaction products and their recyclability, but also the potential improvement of lifetimes due to electron-injection into semiconductors and enhanced selectivity due to catalysis in confined spaces. However, their synthetic applications are still in their infancy. One of the early reports by the group of Lin showed the incorporation of Ru and Ir complexes into a metal-organic framework (MOF, UiO-67) through the dicarboxylic acid functionality on one of the cyclometallated ligands. The PS-doped MOF network was able to act as a heterogenous photocatalyst for water splitting, CO_2 reduction, amine coupling and other photooxidation reactions.[128] Later, the group of Garcia and Ferrer utilized the same Ru-PS incorporated into the MOF structures for the photocatalytic debromination of α-bromoketones into its respective aldehydes.[129] Further, they have studied the mechanistic pathway of the catalysis with optical spectroscopy techniques. Upon excitation, the localized triplet excited state of the Ru(II) bipyridyl complex incorporated MOF decays partly to a very long-lived (millisecond time scale) photoinduced charge-separated state, further proved by the reduction of MV^{2+} as the electron acceptor (Figure 26). The TAS measurement performed for the Ru-MOF powder by the diffused reflectance mode shows characteristic signals of $\mathbf{PS_{Ru}}^*$, *i.e.* positive transient absorption band at 350 nm, the bleaching of the ground state (negative signal at 460 nm) and the emission (negative signal at 640 nm), respectively. At later timescale, a build-up of the new feature centred around 680 nm was also observed, which is distinct from the transient absorption of $\mathbf{PS_{Ru}}^*$. Additionally, the transient kinetics measured at 340 nm, 460 nm, and 600 nm show a distinct kinetic decay. Typically, transient absorption spectra of $\mathbf{PS_{Ru}}$ involve a positive band around 340 nm and a negative bleach around 450 nm and both kinetic decays equally to the ground state in < 1 μs. The presence of distinct decay features, which was also long-lived until 20 ms, invoked the presence of multiple transient species or charge-separated states occurring in MOF materials. This long-lived species, with respect to its analogous TAS measurement for soluble complex alone, was assigned to photo rejected electrons located to the Zr-based MOF cluster. Whereas the positive holes are located to the Ru(III) species for the initial time scale after laser excitation and further migrate to the MOF lattice or reacting with H_2O molecules in ms time. This long-lived transient was further found to be quenched with MV^{2+}, acting as an electron acceptor, followed by the appearance of reduced $MV^{\bullet+}$ spectra in the region

of 500-800 nm. Finally, this long-lived charge-separated state is found to be beneficial for the photoredox catalytic debromination reaction to aldehyde. Apart from these organic reactions, the Ru based PS's incorporated in MOF networks were explored for water[130,131], and CO_2 reduction.[132] Further studies include the photoinduced electron transfer kinetics with transient spectroscopy ranging from ps-s timescale and elucidation of the key intermediates involved in catalytic reduction reactions.

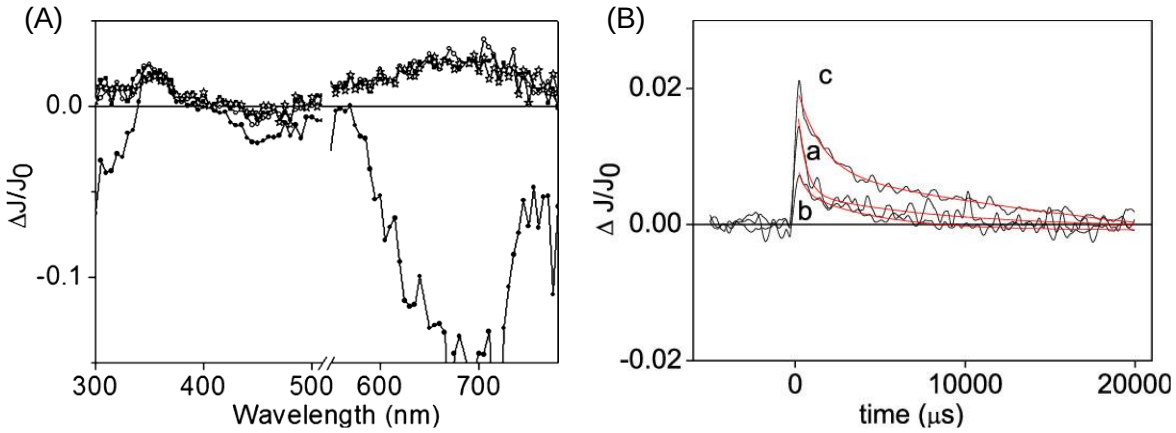

Figure 26: Diffuse reflectance transient absorption spectra of $\mathbf{PS_{Ru}}$ incorporated into UiO-67 (Zr) MOF recorded at 1 (●), 6 (○), 20 (■), and 40 (☆) μs upon 532 nm laser excitation, and its transient absorption kinetics monitored at 340 (a), 460 (b), and 600 nm (c). The red line shows the best fit of the kinetics to a sum of two mono-exponential kinetics. Reproduced with permission from ref.[129]

Similar to the Ru(III) complexes, cyclomatellated Ir(III) complexes were also incorporated into the MOF networks and used as a photocatalyst for C-S bond formation. A dual catalytic strategy was employed by the group of Lin, where $[Ir(C^N)_2(N^N)]^+$ and a Ni(II) based cross-coupling catalyst were mutually incorporated into Zr-based MOF networks to efficiently catalyze C-S bond formation between various aryl iodides and thiols.[133] However, the mechanistic evidence of the catalysis was translated from precedent reports of their homogenous counterpart. The reaction follows *via* the reductive quenching of excited-state $\mathbf{PS_{Ir}}$ by phenyl thiolate substrate and forming the thiophenol radical. The reduced $\mathbf{PS_{Ir}}$ undergoes SET with a closely located Ni(II) complex and proceeds further by oxidative addition of thiophenol radical to form Ni(III) intermediate and reductive elimination of the product diaryl sulfide. The luminescence quenching and thermodynamically feasible redox potential values of reaction partners also support this mechanism.

5. Organometallic iron complexes as analogous d^6 metal photocatalysts

As detailed above, the utilization of Ru(II) and Ir(III) complexes as photocatalyst has been heavily exploited in photoredox catalysis, and now their more earth-abundant analogs like 3d metal complexes are also getting attention. Among this, Fe complexes coordinated with strong field ligands have been reported in electron transfer redox applications. The ligand engineering has enabled similar excited state behavior like Ru or Ir complexes by either stabilizing the MLCT excited state or pushing the metal-centered energy states (e_g), avoiding the fast-excited state deactivation through MC states.[17,134] Alternatively, the group of Sundström, Persson, Lomoth, and Wärnmark have introduced a low spin Fe(III) complex, $[Fe(phtmeimb)_2]^+$, which exhibit room-temperature photoluminescence from ^{2}LMCT excited state with a lifetime of 2.2 ns and a quantum yield of 2% (Figure 27).[135] The strong sigma donating two anionic scorpionate-like tris-carbene ligands in $[Fe(phtmeimb)_2]^+$ destabilize the metal-centred e_g orbitals and results ^{2}LMCT to be emissive in nanosecond timescale. This charge-transfer excited state is also found to act as both strong reductant and oxidant (E_{ox}= 1.9 V and E_{red}=1.0 V, vs. $FC^{+/0}$), which was further proved by reductive quenching with diphenylamine and oxidative quenching with methyl viologen to form $MV^{\bullet+}$ at diffusion-limited rate kinetics.

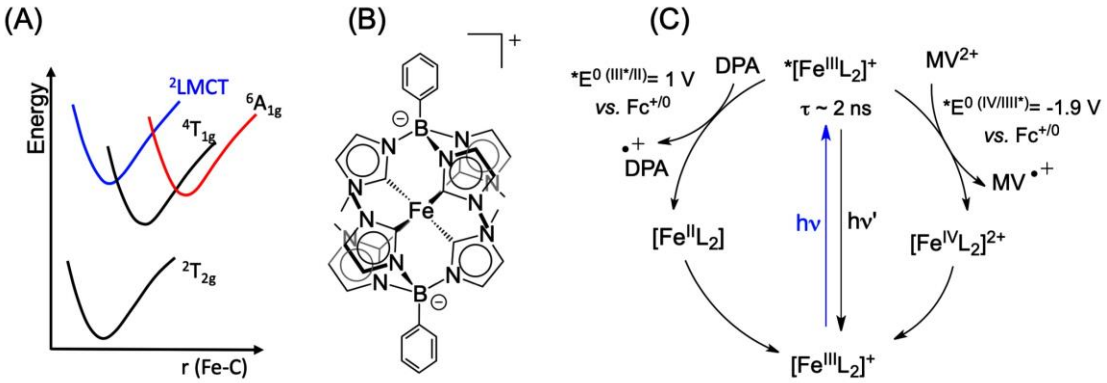

Figure 27: (A) Potential-energy diagram of $[Fe(phtmeimb)_2]^+$, (B) The structure of $[Fe(phtmeimb)_2]^+$ (phtmeimb=$^{40-}$), (C) The oxidative and reductive electron transfer between $[Fe(phtmeimb)_2]^+$ and methyl viologen (MV^{2+}) or diphenyl amine (DPA).

Very recently, the group of McCusker reported a paradigm change in understanding photoredox catalysis with iron complexes, where they have demonstrated redox-active and metal-centred ligand-field excited state present in the iron complex, $[Fe(tren(py)_3)]^{2+}$ (where $tren(py)_3$ = tris(2-pyridyl-methylimino-ethyl)amine).[136] Unlike the isoelectronic Ir- and Ru-based metal complexes, this polypyridyl Fe(II) complex can be photoexcited to yield a high spin metal-centred ligand-field state ($^5T_2$). The reduction redox potential of the $^5T_2$ state of $[Fe(tren\text{-}(py)_3)]^{2+}$ was estimated −0.35 ± 0.05 V (in acetone, *vs.* $Fc^{+/0}$). There is a need for more work to develop iron-based photocatalysts.

6. Conclusion and perspectives

The application of photoredox catalysis in the transformation of small molecules has changed synthetic organic chemistry. An evenly growing community is including photoredox catalysis in their toolbox to solve elusive organic transformations, which were not possible before. The mechanistic proposals of these photocatalytic reactions have been mainly explained by the thermodynamics of electron transfer or by simple luminescence quenching studies. However, the mechanistic aspect of photoredox catalysis is vibrant, and further studies are needed to grasp all potentials of photoredox catalysis, improving photoredox catalysis by the rational design. To this end, a variety of photophysical and photochemical principles well-known in the physical inorganic chemistry field can serve to act as a tool guide for performing detailed mechanistic studies of photocatalytic reactions. The concepts of electron and energy transfer process and the spectroscopic identification of redox equivalents outlined herein are general and can be extrapolated to other studies. We hope that the present review will trigger more studies on the detailed understanding of photoredox reactions.

Conflict of interest

There are no conflicts to declare

Acknowledgement

We thank ICIQ and ICREA for their financial support. Moreover, the authors also acknowledge competitive funding from the European Research Foundation project ERC-2014-CoG 648304 (J.L.-F.), MINECO (CTQ2016-80038-R), and AGAUR 2017-SGR-1647 (J.L.-F.); MINECO (Projects CTQ2013-47183 and CTQ 2017-89814-P), and SGR AGAUR 2017SGR00978 (E.P.). N.K. thank JyC for postdoctoral scholarship.

References

1. B. Zhang and L. Sun, *Chem. Soc. Rev.*, 2019, **48**, 2216-2264.
2. G. Ciamician, *Science*, 1912, **36**, 385-394.
3. N. S. Lewis and D. G. Nocera, *Proc. Natl. Acad. Sci. U. S. A.*, 2006, **103**, 15729-15735.
4. H. B. Gray, *Nat. Chem,*, 2009, **1**, 7.
5. N. Armaroli and V. Balzani, *Chem. Eur. J.*, 2016, **22**, 32-57.
6. S. P. Pitre, C. D. McTiernan and J. C. Scaiano, *Acc. Chem. Res.*, 2016, **49**, 1320-1330.
7. C. K. Prier, D. A. Rankic and D. W. C. MacMillan, *Chem. Rev.*, 2013, **113**, 5322-5363.
8. D. M. Schultz and T. P. Yoon, *Science*, 2014, **343**, 1239176.
9. J. M. Narayanam and C. R. Stephenson, *Chem. Soc. Rev.*, 2011, **40**, 102-113.
10. N. Corrigan, S. Shanmugam, J. Xu and C. Boyer, *Chem. Soc. Rev.*, 2016, **45**, 6165-6212.
11. N. A. Romero and D. A. Nicewicz, *Chem. Rev.*, 2016, **116**, 10075-10166.
12. K. Burkhard, *Chemical Photocatalysis*, De Gruyter, Berlin, Boston, 2020.
13. F. Glaser and O. S. Wenger, *Coord. Chem. Rev.*, 2020, **405**, 213129.
14. A. Hossain, A. Bhattacharyya and O. Reiser, *Science*, 2019, **364**, eaav9713.

15. C. Förster and K. Heinze, *Chem. Soc. Rev.*, 2020, **49**, 1057-1070.
16. O. S. Wenger, *J. Am. Chem. Soc.*, 2018, **140**, 13522-13533.
17. J. K. McCusker, *Science*, 2019, **363**, 484-488.
18. B. M. Hockin, C. Li, N. Robertson and E. Zysman-Colman, *Catalysis Science & Technology*, 2019, **9**, 889-915.
19. C. B. Larsen and O. S. Wenger, *Chem. Eur. J.*, 2018, **24**, 2039-2058.
20. A. K. Pal, C. Li, G. S. Hanan and E. Zysman-Colman, *Angew. Chem. Int. Ed.*, 2018, **57**, 8027-8031.
21. C. R. Stephenson, T. P. Yoon and D. W. MacMillan, *Visible light photocatalysis in organic chemistry*, John Wiley & Sons, 2018.
22. A. Savateev, I. Ghosh, B. König and M. Antonietti, *Angew. Chem. Int. Ed.*, 2018, **57**, 15936-15947.
23. S. I. Ting, S. Garakyaraghi, C. M. Taliaferro, B. J. Shields, G. D. Scholes, F. N. Castellano and A. G. Doyle, *J. Am. Chem. Soc.*, 2020, **142**, 5800-5810.
24. L. Tian, N. A. Till, B. Kudisch, D. W. C. MacMillan and G. D. Scholes, *J. Am. Chem. Soc.*, 2020, **142**, 4555-4559.
25. F. Glaser, C. Kerzig and O. S. Wenger, *Angew. Chem. Int. Ed.*, 2020, **59**, 10266-10284.
26. D. M. Arias-Rotondo and J. K. McCusker, *Chem. Soc. Rev.*, 2016, **45**, 5803-5820.
27. M. Marchini, G. Bergamini, P. G. Cozzi, P. Ceroni and V. Balzani, *Angew. Chem.*, 2017, **129**, 12996-12997.
28. I. Ghosh, J. I. Bardagi and B. König, *Angew. Chem. Int. Ed.*, 2017, **56**, 12822-12824.
29. B. König, *Chemical Photocatalysis*, Walter de Gruyter, 2013.
30. L. Buzzetti, G. E. Crisenza and P. Melchiorre, *Angew. Chem. Int. Ed.*, 2019, **58**, 3730-3747.
31. A. Studer and D. P. Curran, *Angew. Chem. Int. Ed.*, 2016, **55**, 58-102.
32. V. Balzani, P. Ceroni and A. Juris, *Photochemistry and photophysics: concepts, research, applications*, John Wiley & Sons, 2014.
33. V. Balzani, G. Bergamini, S. Campagna and F. Puntoriero, in *Photochemistry and Photophysics of Coordination Compounds I*, eds. V. Balzani and S. Campagna, 2007, vol. 280, pp. 1-36.
34. J. G. Vos and M. T. Pryce, *Coord. Chem. Rev.*, 2010, **254**, 2519-2532.
35. D. M. Roundhill, *Photochemistry and photophysics of metal complexes*, Springer Science & Business Media, 2013.
36. E. I. Solomon and A. B. P. Lever, *Inorganic Electronic Structure and Spectroscopy: Methodology*, Wiley, 2006.
37. O. Horváth and K. L. Stevenson, *Charge transfer photochemistry of coordination compounds*, VCH, 1993.
38. R. C. Evans, P. Douglas and H. D. Burrow, *Applied photochemistry*, Springer, 2013.
39. K. Kalyanasundaram, *Coord. Chem. Rev.*, 1982, **46**, 159-244.
40. E. Zysman-Colman, *Iridium (III) in optoelectronic and photonics applications*, John Wiley & Sons, 2017.
41. K. Kalyanasundaram, *Coord. Chem. Rev.*, 1982, **46**, 159-244.
42. in *Iridium(III) in Optoelectronic and Photonics Applications*, 2017, DOI: https://doi.org/10.1002/9781119007166.ch1, pp. 1-69.
43. in *Iridium(III) in Optoelectronic and Photonics Applications*, 2017, DOI: https://doi.org/10.1002/9781119007166.ch11, pp. 541-581.

44. J. R. Lakowicz, *Principles of Fluorescence Spectroscopy*, Springer US, 2007.
45. G. J. Kavarnos and N. J. Turro, *Chem. Rev.*, 1986, **86**, 401-449.
46. C. R. Bock, J. A. Connor, A. R. Gutierrez, T. J. Meyer, D. G. Whitten, B. P. Sullivan and J. K. Nagle, *J. Am. Chem. Soc.*, 1979, **101**, 4815-4824.
47. W. E. Jones and M. A. Fox, *J. Phys. Chem.*, 1994, **98**, 5095-5099.
48. V. Balzani, *Electron transfer in chemistry*, Vch Verlagsgesellschaft Mbh, 2001.
49. F. Strieth-Kalthoff, M. J. James, M. Teders, L. Pitzer and F. Glorius, *Chem. Soc. Rev.*, 2018, **47**, 7190-7202.
50. M. J. Peach, P. Benfield, T. Helgaker and D. J. Tozer, *The Journal of chemical physics*, 2008, **128**, 044118.
51. J. Zhao, J. L. Brosmer, Q. Tang, Z. Yang, K. Houk, P. L. Diaconescu and O. Kwon, *J. Am. Chem. Soc.*, 2017, **139**, 9807-9810.
52. R. G. W. Norrish and G. Porter, *Nature*, 1949, **164**, 658-658.
53. G.-N. Porter, *Proceedings of the Royal Society of London. Series A. Mathematical and Physical Sciences*, 1950, **200**, 284-300.
54. L. Hammarstrom and S. Hammes-Schiffer, *Acc. Chem. Res.*, 2009, **42**, 1859-1860.
55. N. Elgrishi, M. B. Chambers, X. Wang and M. Fontecave, *Chem. Soc. Rev.*, 2017, **46**, 761-796.
56. A. Juris, V. Balzani, F. Barigelletti, S. Campagna, P. l. Belser and A. v. von Zelewsky, *Coord. Chem. Rev.*, 1988, **84**, 85-277.
57. U. S. Akhtar, E. L. Tae, Y. S. Chun, I. C. Hwang and K. B. Yoon, *ACS Catalysis*, 2016, **6**, 8361-8369.
58. B. H. Farnum, J. J. Jou and G. J. Meyer, *Proc. Natl. Acad. Sci. U. S. A.*, 2012, **109**, 15628-15633.
59. P. Ceroni, G. Bergamini and V. Balzani, *Angew. Chem. Int. Ed.*, 2009, **48**, 8516-8518.
60. S. Fischer, D. Hollmann, S. Tschierlei, M. Karnahl, N. Rockstroh, E. Barsch, P. Schwarzbach, S.-P. Luo, H. Junge and M. Beller, *ACS Catalysis*, 2014, **4**, 1845-1849.
61. O. Ishitani, K. Ishii, S. Yanagida, C. Pac, T. Ohno and A. Yoshimura, *Chem. Lett.*, 1989, **18**, 217-220.
62. S. I. Shylin, M. V. Pavliuk, L. D'Amario, I. O. Fritsky and G. Berggren, *Faraday Discuss.*, 2019, **215**, 162-174.
63. S. San Tan, S. Yanagisawa, K. Inagaki, M. B. Kassim and Y. Morikawa, *Physical Chemistry Chemical Physics*, 2019, **21**, 7973-7988.
64. A. M. Brown, C. E. McCusker and J. K. McCusker, *Dalton Trans.*, 2014, **43**, 17635-17646.
65. A. Company, G. Sabenya, M. Gonzalez-Bejar, L. Gomez, M. Clemancey, G. Blondin, A. J. Jasniewski, M. Puri, W. R. Browne and J.-M. Latour, *J. Am. Chem. Soc.*, 2014, **136**, 4624-4633.
66. S. Fukuzumi, T. Kojima, Y.-M. Lee and W. Nam, *Coord. Chem. Rev.*, 2017, **333**, 44-56.
67. S. Fukuzumi, T. Kishi, H. Kotani, Y.-M. Lee and W. Nam, *Nat. Chem,*, 2011, **3**, 38.
68. H. Kotani, T. Suenobu, Y.-M. Lee, W. Nam and S. Fukuzumi, *J. Am. Chem. Soc.*, 2011, **133**, 3249-3251.
69. C. Saracini, S. Fukuzumi, Y.-M. Lee and W. Nam, *Dalton Trans.*, 2018, **47**, 16019-16026.
70. S. Fukuzumi, T. Mizuno and T. Ojiri, *Chem. Eur. J.*, 2012, **18**, 15794-15804.
71. N. T. Vo, Y. Mekmouche, T. Tron, R. Guillot, F. Banse, Z. Halime, M. Sircoglou, W. Leibl and A. Aukauloo, *Angew. Chem.*, 2019, **131**, 16169-16173.

72. N. T. Vo, Y. Mekmouche, T. Tron, R. Guillot, F. Banse, Z. Halime, M. Sircoglou, W. Leibl and A. Aukauloo, *Angew. Chem. Int. Ed.*, 2019, **58**, 16023-16027.
73. E. P. Farney, S. J. Chapman, W. B. Swords, M. D. Torelli, R. J. Hamers and T. P. Yoon, *J. Am. Chem. Soc.*, 2019, **141**, 6385-6391.
74. J. R. Herance, B. Ferrer, J. L. Bourdelande, J. Marquet and H. Garcia, *Chem. Eur. J.*, 2006, **12**, 3890-3895.
75. R. Naumann, C. Kerzig and M. Goez, *Chem. Sci.*, 2017, **8**, 7510-7520.
76. C. Kerzig and M. Goez, *Chem. Sci.*, 2016, **7**, 3862-3868.
77. C. Kerzig and M. Goez, *Physical Chemistry Chemical Physics*, 2015, **17**, 13829-13836.
78. M. Goez, C. Kerzig and R. Naumann, *Angew. Chem. Int. Ed.*, 2014, **53**, 9914-9916.
79. R. Naumann and M. Goez, *Chem. Eur. J.*, 2018, **24**, 17557-17567.
80. T. R. Blum, Z. D. Miller, D. M. Bates, I. A. Guzei and T. P. Yoon, *Science*, 2016, **354**, 1391-1395.
81. F. M. Hörmann, C. Kerzig, T. S. Chung, A. Bauer, O. S. Wenger and T. Bach, *Angew. Chem. Int. Ed.*, 2020, **59**, 9659-9668.
82. M. Kudisch, C.-H. Lim, P. Thordarson and G. M. Miyake, *J. Am. Chem. Soc.*, 2019, **141**, 19479-19486.
83. I. N. Mills, J. A. Porras and S. Bernhard, *Acc. Chem. Res.*, 2018, **51**, 352-364.
84. M. S. Lowry and S. Bernhard, *Chem. Eur. J.*, 2006, **12**, 7970-7977.
85. R. D. Costa, E. Orti, H. J. Bolink, F. Monti, G. Accorsi and N. Armaroli, *Angew. Chem. Int. Ed.*, 2012, **51**, 8178-8211.
86. I. M. Dixon, J.-P. Collin, J.-P. Sauvage, L. Flamigni, S. Encinas and F. Barigelletti, *Chem. Soc. Rev.*, 2000, **29**, 385-391.
87. Y. You and W. Nam, *Chem. Soc. Rev.*, 2012, **41**, 7061-7084.
88. K.-C. Tang, K. L. Liu and I.-C. Chen, *Chem. Phys. Lett.*, 2004, **386**, 437-441.
89. S. Takayasu, T. Suzuki and K. Shinozaki, *The Journal of Physical Chemistry B*, 2013, **117**, 9449-9456.
90. T. Hofbeck and H. Yersin, *Inorg. Chem.*, 2010, **49**, 9290-9299.
91. D. A. Kurtz and J. L. Dempsey, *Inorg. Chem.*, 2019, **58**, 16510-16517.
92. J. D. Nguyen, E. M. D'amato, J. M. Narayanam and C. R. Stephenson, *Nat. Chem,*, 2012, **4**, 854.
93. T. Kohlmann, R. Naumann, C. Kerzig and M. Goez, *Photochemical & Photobiological Sciences*, 2017, **16**, 1613-1622.
94. R. Naumann, F. Lehmann and M. Goez, *Angew. Chem. Int. Ed.*, 2018, **57**, 1078-1081.
95. C. Kerzig, X. Guo and O. S. Wenger, *J. Am. Chem. Soc.*, 2019, **141**, 2122-2127.
96. T. Kohlmann, C. Kerzig and M. Goez, *Chem. Eur. J.*, 2019, **25**, 9991-9996.
97. M. Giedyk, R. Narobe, S. Weiß, D. Touraud, W. Kunz and B. König, *Nature Catalysis*, 2020, **3**, 40-47.
98. C. Prier, D. Rankic and D. MacMillan, *Science*, 2014, **343**, 1239176-1239171.
99. J.-H. Shon and T. S. Teets, *Comments Inorg. Chem.*, 2019, DOI: 10.1080/02603594.2019.1694517, 1-33.
100. K. W. Shimkin and D. A. Watson, *Beilstein journal of organic chemistry*, 2015, **11**, 2278-2288.
101. J. D. Slinker, A. A. Gorodetsky, M. S. Lowry, J. Wang, S. Parker, R. Rohl, S. Bernhard and G. G. Malliaras, *J. Am. Chem. Soc.*, 2004, **126**, 2763-2767.
102. H. Kim and C. Lee, *Angew. Chem. Int. Ed.*, 2012, **51**, 12303-12306.

103. C.-J. Wallentin, J. D. Nguyen, P. Finkbeiner and C. R. J. Stephenson, *J. Am. Chem. Soc.*, 2012, **134**, 8875-8884.
104. M. S. Lowry, J. I. Goldsmith, J. D. Slinker, R. Rohl, R. A. Pascal, G. G. Malliaras and S. Bernhard, *Chem. Mater.*, 2005, **17**, 5712-5719.
105. E. B. Corcoran, M. T. Pirnot, S. Lin, S. D. Dreher, D. A. DiRocco, I. W. Davies, S. L. Buchwald and D. W. MacMillan, *Science*, 2016, **353**, 279-283.
106. E. Erdmann, A. Villinger, B. König and W. Seidel, *Photochemical & Photobiological Sciences*, 2018, **17**, 1056-1067.
107. D. R. Whang, K. Sakai and S. Y. Park, *Angew. Chem. Int. Ed.*, 2013, **52**, 11612-11615.
108. Y.-J. Yuan, J.-Y. Zhang, Z.-T. Yu, J.-Y. Feng, W.-J. Luo, J.-H. Ye and Z.-G. Zou, *Inorg. Chem.*, 2012, **51**, 4123-4133.
109. S.-y. Takizawa, N. Ikuta, F. Zeng, S. Komaru, S. Sebata and S. Murata, *Inorg. Chem.*, 2016, **55**, 8723-8735.
110. J.-H. Shon, S. Sittel and T. S. Teets, *ACS Catalysis*, 2019, **9**, 8646-8658.
111. J.-H. Shon and T. S. Teets, *Inorg. Chem.*, 2017, **56**, 15295-15303.
112. Z. T. Yu, Y. J. Yuan, J. G. Cai and Z. G. Zou, *Chem. Eur. J.*, 2013, **19**, 1303-1310.
113. S. I. Bokarev, D. Hollmann, A. Pazidis, A. Neubauer, J. Radnik, O. Kühn, S. Lochbrunner, H. Junge, M. Beller and A. Brückner, *Physical Chemistry Chemical Physics*, 2014, **16**, 4789-4796.
114. S. I. Bokarev, O. S. Bokareva and O. Kuehn, *Coord. Chem. Rev.*, 2015, **304**, 133-145.
115. A. Call, Z. Codolà, F. Acuña‐Parés and J. Lloret‐Fillol, *Chem. Eur. J.*, 2014, **20**, 6171-6183.
116. A. Call, F. Franco, N. Kandoth, S. Fernández, M. González-Béjar, J. Pérez-Prieto, J. M. Luis and J. Lloret-Fillol, *Chem. Sci.*, 2018, **9**, 2609-2619.
117. S. Ruccolo, Y. Qin, C. Schnedermann and D. G. Nocera, *J. Am. Chem. Soc.*, 2018, **140**, 14926-14937.
118. D. C. Miller, G. J. Choi, H. S. Orbe and R. R. Knowles, *J. Am. Chem. Soc.*, 2015, **137**, 13492-13495.
119. R. Sun, Y. Qin, S. Ruccolo, C. Schnedermann, C. Costentin and D. G. Nocera, *J. Am. Chem. Soc.*, 2018, **141**, 89-93.
120. E. R. Welin, C. Le, D. M. Arias-Rotondo, J. K. McCusker and D. W. C. MacMillan, *Science*, 2017, **355**, 380.
121. M. Teders, C. Henkel, L. Anhäuser, F. Strieth-Kalthoff, A. Gómez-Suárez, R. Kleinmans, A. Kahnt, A. Rentmeister, D. Guldi and F. Glorius, *Nat. Chem.*, 2018, **10**, 981-988.
122. I. Ghosh, J. Khamrai, A. Savateev, N. Shlapakov, M. Antonietti and B. König, *Science*, 2019, **365**, 360-366.
123. S. H. Bossmann, S. Jockusch, P. Schwarz, B. Baumeister, S. Göb, C. Schnabel, L. Payawan Jr, M. R. Pokhrel, M. Wörner and A. M. Braun, *Photochemical & Photobiological Sciences*, 2003, **2**, 477-486.
124. K. Mori, M. Kawashima, M. Che and H. Yamashita, *Angew. Chem. Int. Ed.*, 2010, **49**, 8598-8601.
125. S. H. Bossmann, C. Turro, C. Schnabel, M. R. Pokhrel, L. M. Payawan, B. Baumeister and M. Wörner, *The Journal of Physical Chemistry B*, 2001, **105**, 5374-5382.
126. X. Deng, Z. Li and H. García, *Chem. Eur. J.*, 2017, **23**, 11189-11209.
127. X. Lang, X. Chen and J. Zhao, *Chem. Soc. Rev.*, 2014, **43**, 473-486.
128. C. Wang, Z. Xie, K. E. deKrafft and W. Lin, *J. Am. Chem. Soc.*, 2011, **133**, 13445-13454.

129. A. Santiago-Portillo, H. G. Baldoví, E. Carbonell, S. Navalón, M. Álvaro, H. García and B. Ferrer, *J. Phys. Chem. C*, 2018, **122**, 29190-29199.
130. C.-C. Hou, T.-T. Li, S. Cao, Y. Chen and W.-F. Fu, *Journal of Materials Chemistry A*, 2015, **3**, 10386-10394.
131. S. Yang, B. Pattengale, S. Lee and J. Huang, *ACS Energy Letters*, 2018, **3**, 532-539.
132. M. Elcheikh Mahmoud, H. Audi, A. Assoud, T. H. Ghaddar and M. Hmadeh, *J. Am. Chem. Soc.*, 2019, **141**, 7115-7121.
133. Y. Y. Zhu, G. Lan, Y. Fan, S. S. Veroneau, Y. Song, D. Micheroni and W. Lin, *Angew. Chem. Int. Ed.*, 2018, **57**, 14090-14094.
134. O. S. Wenger, *Chem. Eur. J.*, 2019, **25**, 6043-6052.
135. K. S. Kjær, N. Kaul, O. Prakash, P. Chábera, N. W. Rosemann, A. Honarfar, O. Gordivska, L. A. Fredin, K.-E. Bergquist, L. Häggström, T. Ericsson, L. Lindh, A. Yartsev, S. Styring, P. Huang, J. Uhlig, J. Bendix, D. Strand, V. Sundström, P. Persson, R. Lomoth and K. Wärnmark, *Science*, 2019, **363**, 249-253.
136. M. D. Woodhouse and J. K. McCusker, *J. Am. Chem. Soc.*, 2020, **142**, 16229-16233.